Università degli Studi di Bologna

FACOLTÀ DI SCIENZE MATEMATICHE, FISICHE E NATURALI

Dipartimento di Fisica - Settore di Geofisica

Dottorato di Ricerca in Fisica
XII° Ciclo

An exhaustive analysis of the Double Torsion method for sub-critical crack propagation in lava rocks and its implications for the understanding of earthquake physics

Tesi di dottorato di:

Dott. Matteo Ciccotti

Relatore:

Prof. Francesco Mulargia

Tutore:

Prof. Maurizio Bonafede

Coordinatore:

Prof. Giulio Pozzi

Anno accademico 1998 - '99

Contents

Acknowledgements

The first person I would like to thank is certainly Professor Francesco Mulargia, with whom the collaboration has been very tight in last three years, and who taught me a wise attitude of criticism.

Then I will thank Dr. Nicola Negri and Lorena Sassi for their important cooperation in the measuring process, Dr. Guido Gonzato for his unlimited informatical knowledge, and Mr. Massimo Bacchetti for skilfully machining the lava rock specimens.

I wish to thank my parents for their evening telephonic moral support (it's not nice to mention the finantial one!), and all my friends for the good time!

This study was performed with contributions of EEC grant EV–5V–CT 92–0190 and CNR, Gruppo Nazionale per la Vulcanologia.

We wish to thank the CINECA computing center in Bologna which provided powerful computing resources and technical support.

This work was accompanied by three articles that were submitted to international reviews in 1999 [7], [8], [9]. The first one was alreay accepted and is now in press.

Chapter 1

Introduction

1.1 The earthquake Physics

Two centuries ago Montessus de Ballore had already concluded that crustal faulting was the basic phenomenon causing earthquakes. However, it is only in the sixties that a quantitative description in terms of radiation field was enounced by Haskell, who transported the results that had been developed at the start of the century by the applied mathematicians to solve engineering problems concerning metals. Comparison with real seismograms, besides allowing accurate radiography of Earth interior, has led to asymptotic solutions for the single event generation mechanism that are satisfactory in the low frequency limit. Nevertheless, the Physics of how and why earthquakes happen remains unknown.

Several processes appear to be potentially important: the state of strain, local mechanical properties, fault geometry, the role of fluids, propagation dynamics, triggering by external elastic waves, thermodynamic conditions. Only the first process was effectively considered in modeling, and mostly in deterministic way. This prevented from reproducing even the most simple and universally accepted characteristics of earthquake occurrence, notably the presence of scaling laws in their distribution, and the trend to clustering in fore-, after-, and mainshocks.

1.1.1 Statistical models

Recent development of models based on statistical mechanics and computer experiments has inspired new hopes of the feasibility of modeling earthquake Physics. These models consider the earth crust as a thermodynamic ensemble that is always near a phase transition (Self Organized Criticality), or that stands for a long time near a phase transition when large earthquakes

occur (Organized Criticality, percolation, etc.). Such models consider single fault dynamics, fault interactions, and sometimes fault geometry, more realistically than the classical ones. Some important dynamic features of seismicity may thus be reproduced, but solutions are not unique and the general contribution to the "understanding" of this phenomenon is still modest. A plethora of models exists and there is no clear idea on how to chose among them.

The unavowed hope is to reduce the problem to some simple deterministic equations with a low number of variables, and to luckily guess their functional form, following the chimera of low-dimensional deterministic chaos. Anyway, the latter seems very unlikely, due to the huge number of variables present in this system.

At the same time, describing a system through statistical mechanics may be a sound approach at equilibrium or, on stationary systems. Serious doubts exist about equilibrium in the earth crust. Furthermore, a description in terms of average quantities appears of modest interest for earthquakes, since single events are important rather than first integrals.

1.1.2 A poor phenomenology

The real problem seems to be the lack of a clear phenomenology. The bulk of the experimental data on which models should potentially be validated is huge and not homogeneous. This data is often based on inferences that lead to theories essentially in contrast with each other. Their continuous and frantic appearance is feeding a worrisome state of confusion instead of leading to some solution.

On the other hand, material rupturing is surely one of the most complicate problems of Physics, and its variables relative to the Earth crust are generally not accessible.

1.1.3 Let's move to the laboratory

A logical approach seems to analyze the problem moving it into a laboratory environment. This is possible, provided that an efficient design allows to reproduce *in situ* the real situation. Up to now, nobody succeeded in this goal.

The basis of laboratory experiments, meant to accurately reproduce the basic mechanisms of crustal seismicity, is the ability of starting and propagating fractures in a stable and controlled fashion. The double torsion loading configuration seems to be the best approach, and has been universally used for measuring fracture parameters since early seventies.

In the Rock Mechanics Laboratory of the Physics Department of the University of Bologna, a sturdy loading machine has been set up, and the skills necessary to perform experiments on subcritical crack propagation in lava rock samples have been developed. Fracture parameters were thus determined for lava rocks coming from Etna, Vulcano, and Stromboli volcanos (Italy).

1.1.4 Is the method accurate?

All the assumptions of the method have been subjected to a careful examination and several stages of the measuring process and data analysis have been optimized with the aim of reducing the traditional variability affecting all measures of fracture parameters in heterogeneous materials.

The classical model used for the interpretation of the test was also examined, since it was essentially based on an analytical formulation, the accuracy of which was indirectly validated in a narrow operational range. We exhaustively addressed the problem by developing a detailed three-dimensional finite-element model to study the effect of several geometric parameters of the specimen.

This study allowed us to identify and correct some substantial inaccuracies in the method, due to the use of the analytical equation. A wide operational range has been thus defined, in which fracture parameters can be accurately measured and controlled.

Chapter 2

Basic fracture mechanics

2.1 Background

Volcanic rocks are mainly present at the surface of the Earth crust. The values of stress and strain that they are subjected to are rather small and their temperature is sufficiently low for these rocks to behave in a fragile way as described by fracture mechanics.

In essence, fracture mechanics concerns the study of stress concentrations caused by sharp-tipped flaws and the conditions for the propagation of these flaws. A criterion based on plausible physical grounds or experimental evidence is used to determine whether a crack or discontinuity will propagate or heal. This is in marked contrast to the historically popular approach in earthquake research of using simple results from the theory of dislocations in elastic solids. In this approach the relative motion on the surface of cracks or discontinuities is assumed *a priori*. With regard to the analysis of the stresses and displacements associated with the crack growth or relative displacement on the surface of a discontinuity the two approaches are essentially coincident.

The analysis of crack problems through fracture mechanics has its roots in attempts to understand the failure of glass, the stability of metal engineering structures, and, more recently, the fracture properties of engineering ceramics. Fracture mechanics has grown particularly because of the success of its relatively simple criteria in describing the failure of these materials. Introduction to the theory and its application to engineering materials can be found in Knott [17], Lawn and Wilshaw [19], and Liebowitz [20].

Recent years have seen a dramatic increase in the attention paid to both experimental fracture mechanics of rocks and the application of fracture mechanics to help to solve fracture problems in geophysics.

The explosion of rock fracture mechanics research has touched many diverse areas including earthquake mechanics, earthquake prediction, plate tectonics, propagating oceanic rifts, magmatic intrusions and their associated earthquakes, uplift and erosion of crustal rocks, hydraulic fracturing and *in situ* stress determination, hot dry rock geothermal energy extraction, crevasse penetration and other glaciological problems, the development of steeply dipping extensional fractures that are nearly ubiquitous at the Earth surface and are formed through folding, upwarping and rifting, fluid transport properties of fracturing rock masses, and the modeling of time-dependent rock failure. A detailed bibliography can be found in Atkinson [4].

2.2 Basic concepts

Fracture mechanics largely derives from the now classic papers of Griffith [13] and Irwin [15] in which the crack as a stress concentrator is accorded its rightful importance in controlling brittle fracture. Fracture mechanics provides a quantitative treatment, based on stress analysis, which relates fracture strength to the applied load and structural geometry of a component containing defects.

The defect is usually modeled as a crack, but it could be a pore or other non-linear defect. The influence of applied loads on crack extension can be described in terms of certain parameters which characterize the stress and strain intensity near the crack tip.

Fracture mechanics was originally concerned with *when* the fracture occurs rather than *why* it occurs.

2.2.1 Crack tip displacement modes

We start with the concept of an ideal flat, perfectly sharp crack of zero thickness and note that there are three basic modes of crack tip displacement 2.1. These are termed mode I, tensile, mode II, in-plane shear, and mode III, out-of-plane shear. In problems concerning crack loading, the superposition of these three basic modes is sufficient to describe the most general case of crack tip deformation and stress field.

If we assume Cartesian coordinates (Fig. 2.2) then on the plane $y = 0$

for mode I: $\sigma_x = 0 \quad \sigma_y \neq \sigma_z = 0 \quad \tau_{xy} = 0$

for mode II: $\tau_{xy} \neq 0 \quad \sigma_y = 0$

for mode III: $\tau_{yz} \neq 0 \quad \sigma_y = 0 \quad \tau_{xy} = 0$

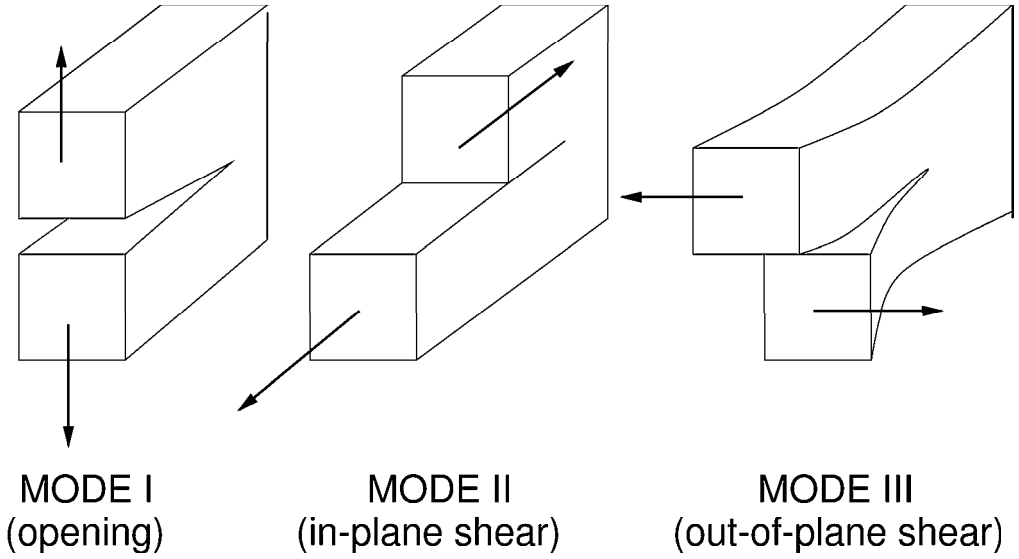

Figure 2.1: Schematic drawing illustrating the three fundamental modes of fracture. Mode I, tensile or opening mode; Mode II, in-plane shear or sliding mode; Mode III, out-of-plane shear or tearing mode.

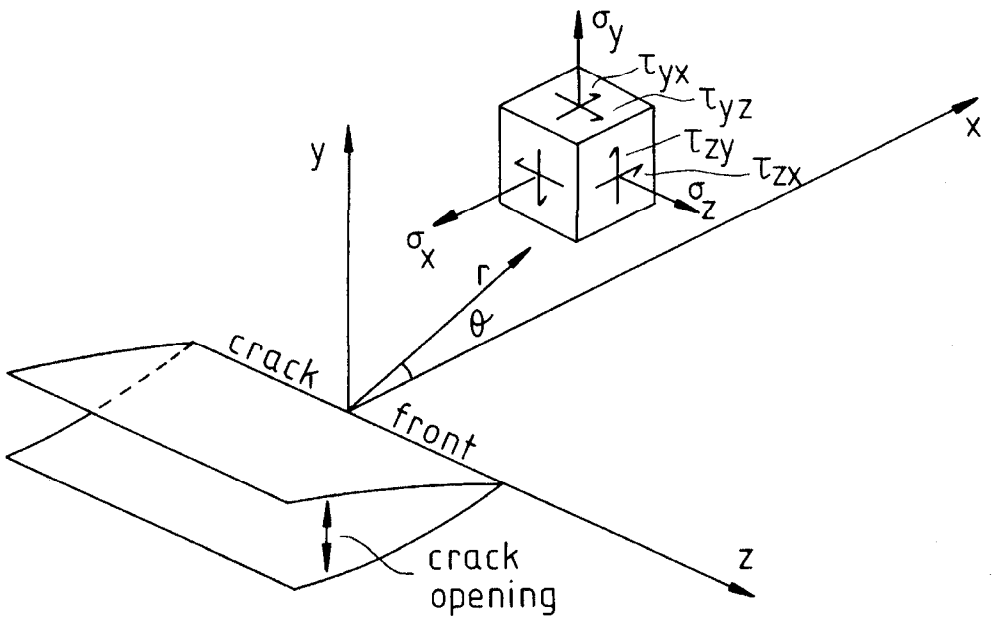

Figure 2.2: Coordinates frames for analyses of linear elastic crack tip stress field. A mode I, tensile crack is shown as an example. The opening of this crack is exaggerated as the sharp-slit approximation is an integral part of the linear elastic analysis.

2.2.2 Stress intensity factor

Stress intensity analysis aims to give a measure of the real forces applied to a crack tip, which will determine whether it will grow or remain stable. These cannot be deduced merely from the external loading conditions.

The stress distribution in the crack tip region is analyzed on the assumption that classical linear theory of elasticity applies. This is valid provided that any region of non-linear behaviour is negligibly small compared with the length of the crack and the dimensions of the cracked body. It is recognized, however, that non-elastic effects and non-linear elastic effects are involved at crack tips in many materials. When these effects become large, fracture mechanics can deal with them by invoking alternative analyses (see § 2.2.4).

Figure 2.2 shows the stress components in the crack tip stress field. In a homogeneous, linear elastic medium the stresses near the crack tip are proportional to $r^{-1/2}$, where r is the distance measured from the crack tip. The coefficient of the $r^{-1/2}$ term in the stress is termed the stress intensity factor and it depends on such factors as the applied load, the shape of the body and the crack length. The stress intensity factor, K, is thus the magnitude of the crack tip stress field for a particular mode in a homogeneous linear elastic material.

Assuming cylindrical coordinates, r, θ, and z shown in Fig. 2.2, linear elastic stress analysis and an isotropic solid, the stresses close to the crack tip for mode I loading are given by

$$\sigma_x = \frac{K_I}{\sqrt{2\pi r}} \, cos\frac{\theta}{2} \left(1 + sin\frac{\theta}{2} \, sin\frac{3\theta}{2}\right) \tag{2.1}$$

$$\sigma_y = \frac{K_I}{\sqrt{2\pi r}} \, cos\frac{\theta}{2} \left(1 - sin\frac{\theta}{2} \, sin\frac{3\theta}{2}\right) \tag{2.2}$$

$$\tau_{xy} = \frac{K_I}{\sqrt{2\pi r}} \, cos\frac{\theta}{2} \, sin\frac{\theta}{2} \, cos\frac{3\theta}{2} \tag{2.3}$$

See [4] for a similar analysis of shear cracks (modes II and III). The K value for mode I can be further defined as

$$K_I = lim[\sigma_y\sqrt{2\pi r}] \qquad as \; r \to 0 \; on \; \theta = 0 \tag{2.4}$$

where σ_y is the tensile stress normal to the crack surface. Similar definitions are obtained for the mode II and mode III K values by replacing σ_y in equation 2.4 with τ_{xy} and τ_{yz}, respectively. A completely general expression for the near field stress distribution for any mode is given by Lawn and Wilshaw [19] as

$$\sigma_{ij} = \frac{K_L}{\sqrt{2\pi r}} f_{ij}(\theta) \tag{2.5}$$

where $f_{ij}(\theta)$ is a well defined function of θ and depends upon the loading mode, and K is the stress intensity factor which embodies the loading configuration and essential boundary conditions of the crack system. The subscript L to K denotes the mode of loading, L = I, II, or III. It is common to simplify stress intensity analysis by assuming that the cracked body has a two-dimensional stress/strain field at the crack tip that does not change along the z direction. For a two-dimensional crack in any mode the stress intensity factor is given by

$$K = Y\sigma_r\sqrt{\pi a} \tag{2.6}$$

where σ_r is the remote applied stress, Y is a numerical modification factor to account for crack geometry, loading conditions, and edge effects, and a for penny-shaped, internal cracks is half the crack length.

2.2.3 Strain energy release rate

Instead of considering crack tip stresses, an alternative fracture mechanics approach to crack extension is to examine the strain energy release rate, or crack extension force, G. Although most contributions to G will come from the crack tip region, it is a global, rather than a local, parameter and includes contributions from all parts of the system (cracked specimen plus loading mechanism). The strain energy release rate is the loss of energy per unit of new crack separation area formed during an increment of crack extension. Because G is calculated for infinitesimal increments of new separation area it can be applied to both stationary and running cracks. Note that strain energy release rate is a rate with respect to crack length and not with respect to time.

For fracture in each of the three fundamental modes of crack tip displacement (Fig. 2.1), the crack extension force for plane strain and assuming linear elasticity is given by

$$G_I = \frac{K_I^2(1-\nu^2)}{E} \tag{2.7}$$

$$G_{II} = \frac{K_{II}^2(1-\nu^2)}{E} \tag{2.8}$$

$$G_{III} = \frac{K_{III}^2}{2\mu} = \frac{K_{II}^2(1+\nu)}{E} \tag{2.9}$$

where ν is Poisson's ratio, E is Young's modulus and μ is the shear modulus. For plane stress the factor $(1-\nu^2)$ in Equations (2.7) and (2.8) is replaced by unity. For the dynamic stress field of a running crack the proportionality factor between G and K^2 is influenced by the crack speed.

2.2.4 J integral

This parameter can be very useful when some sort of non-linear elastic or inelastic process in the crack tip region makes a significant contribution to the energetics of fracture. For the crack system shown in 2.2 the J integral is defined as

$$J = \int_{\Gamma} (W n_x - n_i \sigma_{ij} \partial U_{ij}/\partial x) ds \qquad i,j = x,y \tag{2.10}$$

where σ_{ij}, and u_{ij} are the stress and displacement components, respectively, and the strain energy density, W is given by

$$W = \int_0^{e_{ij}} \sigma_{ij} de_{ij} \tag{2.11}$$

s is the arc length and n_i are the components of the unit normal to the contour or path of integration, Γ, which begins and ends on the crack surfaces and encloses the crack tip. For linear or non-linear elastic materials which are homogeneous in the x direction the value of J is path-independent. Thus, evaluation of J on a remote contour and on one near the crack tip enables conditions at the crack tip to be related to parameters describing the applied loads.

The J integral can also be determined by an energy rate interpretation where

$$J = -dU/dA = G \qquad y = constant \tag{2.12}$$

where U is the total strain energy of the system, A is the crack surface area and y is the displacement of the applied force. Thus, J is identical to the strain energy release rate, G, in the case of linear elastic stress-strain behaviour or small scale yielding. It is most widely used, however, for the characterization of crack tip conditions in the case of large scale yielding.

2.3 Crack extension laws

There are two types of crack extension laws in fracture mechanics.

Equilibrium laws, which specify that cracks may extend stably or unstably at some critical value of a fracture mechanics parameter (K_c, G_c, J_c).

Kinetic laws, in which at certain subcritical values of fracture mechanics parameters a crack can extend at a velocity which is a function of the magnitude of the crack driving force. The most important example of kinetic crack growth from the standpoint of geophysics is that due to chemical interaction between crack tip material and environmental species (stress-corrosion).

2.3.1 Equilibrium laws

A key concept in the widespread use of fracture mechanics is that extension of a fracture will occur once a critical value of stress intensity factor, K_c, or crack extension force, G_c, has been reached or exceeded. There is a vast literature on the fracture of glass, ceramics and metals to show that this concept has found very widespread practical application in engineering. Once the critical value of K or G has been reached, crack propagation is known as fast or catastrophic fracture because its speed can approach that of sound in the medium provided that the crack is isolated and its walls are traction free. If we consider purely tensile loading, G_c is related to the Griffith energy balance concept by

$$G_c = 2Q_f \geq 2Q_s \tag{2.13}$$

where Q_f is the tensile fracture surface energy or global fracture resistance term. The fracture surface energy is generally greater than the ideal or thermodynamic surface energy, Q_s, which in an ideally brittle solid is merely the work done in separating material across neighbouring atomic planes. This is because various energy dissipation processes operate at crack tips in many solids, other than those processes associated purely with new surface formation. These additional processes include crack tip microplasticity and acoustic emission, and they are all included in the calculation of the fracture surface energy.

2.3.2 Kinetic laws

The equilibrium approach to crack extension is not a sufficiently general view of crack growth during long-term loading, a condition that is of particular interest in geophysics. It is found in experiments on a wide range of materials that significant rates of crack growth can occur at values of K or

G often far below the critical values of these parameters. This is known as *subcritical crack growth.* Where chemical weakening of crack tips by environmental species occurs it is known as *stress-corrosion.* But other mechanisms can contribute such as dissolution, diffusion, ion exchange and microplasticity. There are numerous kinetic laws for crack extension, all sharing the common form

$$v = v(K, G) \tag{2.14}$$

where v is the crack velocity. The specific form of the crack velocity dependence on K or G depends on the precise mechanism whereby the energy barrier to crack extension is overcome. Sometimes the form of this dependence is assumed from experimental results and sometimes from physico-chemical theories regarding the assumed crack tip weakening process.

It is usually assumed, although rarely measured in experiments, that crack growth ceases below some small value of G or K termed *stress-corrosion limit*, $(G, K)_0$. The detailed form of the $v(G, K)$ curve between $(G, K)_0$ and $(G, K)_c$ depends on the specific mechanism or mechanisms of subcritical crack growth. For what concerns rocks, a typical three-stage behavior can be observed (see Fig. 2.3). Each linear region can be described by the well known Charles power low [6]:

$$v = v_0 exp\left(-\frac{H}{RT}\right) K^n \tag{2.15}$$

where H is the activation enthalpy, R is the gas constant, T is the absolute temperature, and v_0 and n are constants. The exponent n is generally known as the *stress corrosion* or *subcritical crack growth index.* In each region crack growth is governed by different mechanisms [10]:

Region I: for low values of G, K. The velocity of crack growth is controlled by the rate of stress corrosion reactions at the crack tip. The slope is positive.

Region II: for intermediate values of G, K. The velocity of crack growth is almost constant since it is limited by the rate of transport of reactive species to crack tip.

Region III: for large values of G, K. Crack growth is mainly controlled by mechanical rupture, following a thermally activated process that is relatively insensitive to the chemical environment.

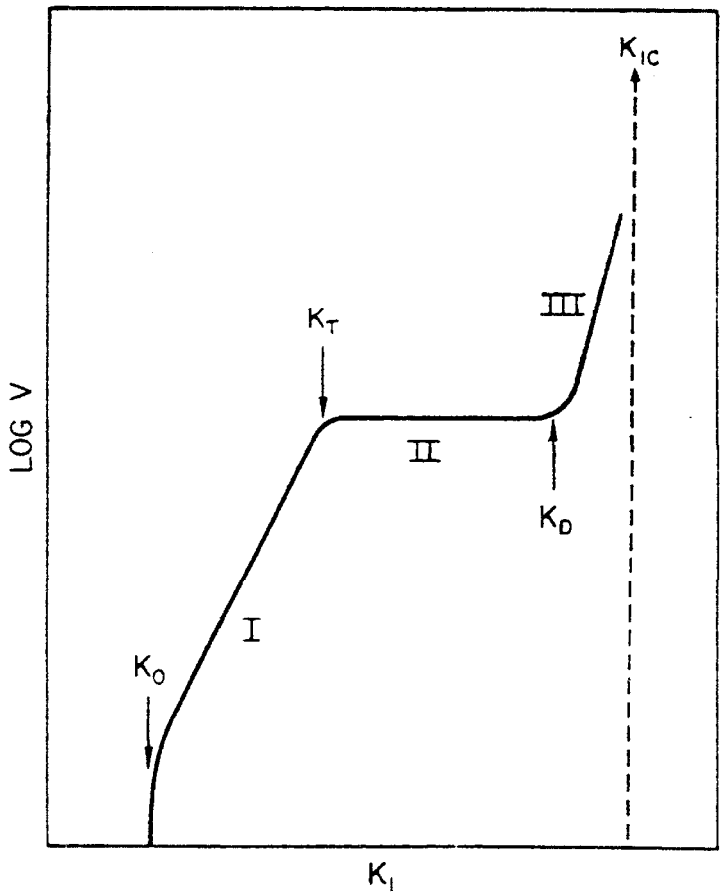

Figure 2.3: Schematic drawing of crack velocity versus crack driving force (expressed as stress intensity factor, K, or strain energy release rate, G) behaviour for ceramics, glasses and rocks. Note the bilogarithmic frame.

Subcritical crack growth is not predicted by classical fracture mechanics. Rice [28] has re-examined the thermodynamics of Griffith-type crack growth, however, and shown that it is governed by

$$(G - 2Q_s)v \geq 0 \tag{2.16}$$

If G is greater than the surface energy $2Q_s$, then the crack will grow. If, on the contrary, G is reduced below $2Q_s$, then *crack healing*, negative values of v, is allowed. This is a particularly important result for the mechanics of the Earth crust where healing of pre-existing cracks is ubiquitous.

2.4 Equivalence of fracture mechanics parameters

Under conditions of small scale yielding the various fracture mechanics parameters can be considered as equivalent. For example, in plane-strain mode I crack propagation

$$G_c = J_c = 2Q_f = K_c^2(1-\nu^2)/E \tag{2.17}$$

It must be emphasized, however, that this equivalence only holds if the assumption of linear elasticity is valid, i.e. any inelastic or non-linear elastic region is confined to a negligibly small zone at the crack tip, and there is no frictional loading on the crack surfaces. Under these circumstances the several parameters in Eq. (2.17) are termed the *fracture toughness* and the material obeys linear elastic fracture mechanics (LEFM). If linear elasticity is not an adequate representation of crack tip behaviour the relations in Eq. (2.17) do not hold and the most appropriate single parameter is chosen as a fracture criterion, e. g. J_c in the case of elastic-plastic behaviour.

2.5 Process zone

Classical fracture mechanics deals with a single, ideal atomically sharp crack. This is a suitable representation for single crystals or at a microscopic level in polycrystalline materials. In these cases extensive electron optical studies have supported the assertion that brittle cracks are atomically sharp and propagate by the sequential rupture of bonds [18]. At a more macroscopic level of study, however, real polycrystalline, polyphase materials such as rocks and ceramics, show more complex behaviour. On loading the blunt, machined notch in Fig. 2.4 a few isolated microcracks are formed, but the system behaviour remains linear.

On further loading the intensity of microcracking increases and behaviour in the crack tip region becomes non-linear. Finally, macrocrack extension occurs because of the linking of microcracks in this non-linear zone, known as the process zone. The macrocrack propagates by taking with it a cloud of damage contained in the process zone. In some materials the process zone may be small with respect to the dimensions of the cracked body and hence a fracture mechanics analysis assuming linear elasticity will still be valid. If the process zone size becomes large then non-linear fracture mechanics analyses are required, such as the J integral. The use of the term process zone is linked above to the development of crack tip microcracking. In the fracture

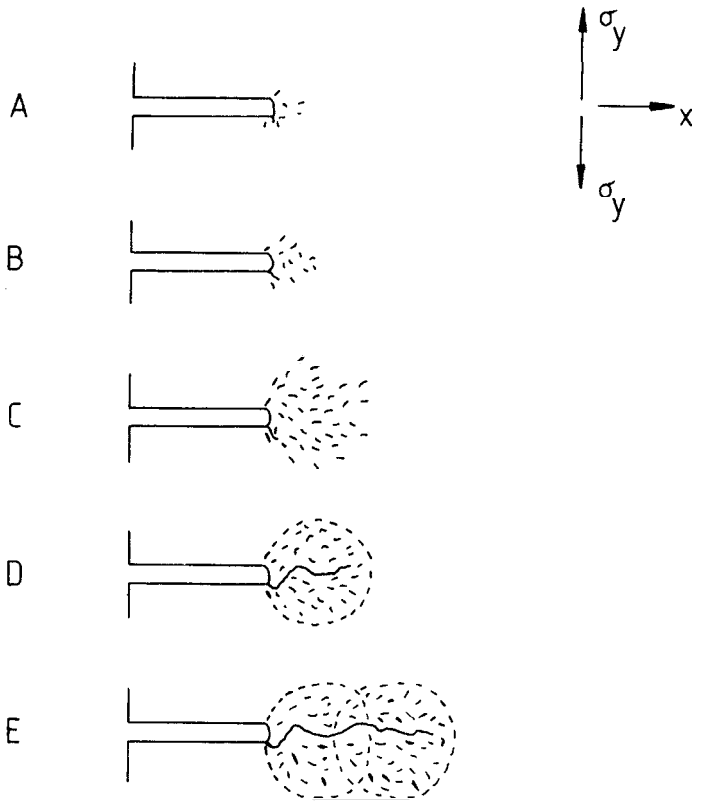

Figure 2.4: Schematic drawings illustrating the development of a process zone and its influence on macrocrack growth. Simple tensile deformation across the plane $y = 0$. Stress increases through drawings A to E. (A) Machined notch with a few isolated microcracks induced by machining. (B) Microcracking begins. Microcracks mostly isolated and linear elastic behaviour is still observed. (C) Microcracking becomes more intense. Some microcracks link up. Non-linear behaviour is observed. (D) Within the now fully developed zone of non- linear elasticity or process zone the macrocrack extends by linking of microcracks. (E) Further macrocrack extension occurs by migration of the process zone through the material ahead of the macrocrack tip. The 'cloud' of microcracks allows macrocrack extension as described above.

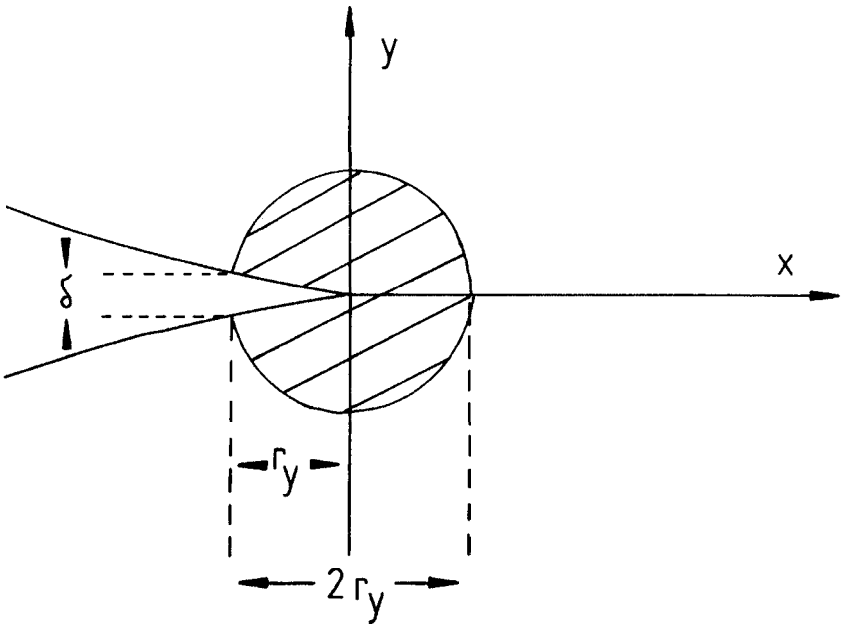

Figure 2.5: Schematic drawing of a nominal plastic zone, non-linear zone, or process zone size, $2r_y$. For simplicity, it is assumed that this zone is circular in the xy plane, although in practice it will depend upon the stress state. The drawing shows simple tensile deformation where a stress, σ_y, acts across the plane $y = 0$.

mechanics literature, however, it is given a more general meaning as any zone of non-linear behaviour at a crack tip. Plasticity, instead of microcracking, could be the means by which the non-linearity is obtained. For large process (microcracking or plasticity) zones the material behaves as if it has a slightly longer macrocrack than is actually measured. K and G determinations can be extended to include a process zone adjustment in the calculation of an effective crack length. If the process zone is idealized as circular in the xy plane (Fig. 2.5) then the adjustment is given by r_y, where

$$r_y = \frac{1}{2\pi}\frac{K^2}{\sigma_y} \tag{2.18}$$

where σ_y is the yield stress. Equation (2.18) is strictly only valid for the case of a process zone involving plasticity, but it is often possible to substitute an effective yield stress for non-plastic materials [30].

2.6 Evaluation of fracture mechanics parameters for specific crack systems

Two distinct methods are used to evaluate fracture mechanics parameters for specific crack systems: (1) stress analysis, and (2) direct measurement using compliance calibrations.

In stress analysis the standard approach is to define a suitable stress function which satisfies the biharmonic equation of linear elasticity theory in accord with the appropriate boundary conditions. This is a fourth-order differential equation embodying the conditions of equilibrium, compatibility of strains, and Hooke's law. The components of stress and strain can be determined from the stress function. For complicated crack systems the analysis is formidable and simplifying analytical techniques are usually invoked, such as the sharp slit approximation of cracks, as discussed by Irwin [15], and Lawn and Wilshaw [19], or the assumption of plane strain or plane stress (for definitions see Jaeger and Cook [16]). In these analyses K terms are introduced to embody the essential boundary conditions of the crack systems.

G and J are usually evaluated experimentally by means of compliance calibrations. Compliance, C, is defined as the displacement of the force application region, y, divided by the applied force, P. Because the strain energy release during incremental crack extension is independent of loading configuration [19]

$$G_P = \frac{1}{2} P^2 \frac{dC}{da} \qquad P = constant \tag{2.19}$$

$$G_y = \frac{1}{2} \frac{y^2}{C^2} \frac{dC}{da} \qquad y = constant \tag{2.20}$$

we have a means of determining G through measuring compliance as a function of crack length to obtain dC/da as a function of a. K can be obtained from Equation (2.17) when this relation is valid. Once a suitable means of calculating K, G or J for a specific crack system has been obtained and an appropriate experimental arrangement has been established, then certain key conditions need to be satisfied before the experimental determination of the parameter is valid. This results from embodying numerous simplifications in the crack analysis. For metals there are certain well defined standards, such as ASTM E399 [1] and E561. No such standard exists for the experimental study of fracture in ceramics or rocks. This has hindered the widespread use of fracture mechanics in geophysics. Various committees of ASTM and the International Society for Rock Mechanics are working towards such standards. Limitations to rock fracture mechanics experimental methods are

discussed by Ouchterlony [22], Atkinson [3] and by Atkinson and Meredith [4].

2.7 Experimental methods

There exists several specimens that can be used for the measurement of fracture parameters in rock materials, but currently no standard technique has yet been defined.

The Commission on Testing Methods of the International Society for Rock Mechanics (ISRM) is drafting a "Suggested method for determining fracture toughness of rock material". The suggested method makes use of either of the chevron-notched specimens shown in Fig. 2.6, and is limited to mode I crack propagation only. Details of this technique may be found in Ouchterlony [24].

No standard technique for fracture toughness testing in modes II and III, or for subcritical crack growth studies in any mode, either exists or is in an active state of development [4]. Nevertheless, a wide range of experimental methods have been used to determine catastrophic crack growth parameters (K_{Ic}, G_{Ic}, J_{Ic}, Q_f) for brittle materials in mode I. A comprehensive review of fracture toughness testing methods for rocks can be found in Ouchterlony [22], [23].

In contrast, only a few methods have been used to study subcritical crack growth. In part, this stems from the great difficulty experienced in determining the position with respect to time of a microcrack tip, especially in opaque polycrystalline rocks, and hence crack velocity.

The vast majority of subcritical crack growth studies on rocks have used the Double-Torsion (DT) testing method. The main advantage of this over other techniques is that crack velocity determinations can be made without the need for multiple crack length measurements when the crack driving load is applied in a particular way. The details of this method will be described in next chapter.

Other specimens that have been used are the Single Edge Notched Beam ($SENB$) in bending (Fig. 2.7) and the Double Cantilever Beam (DCB) (Fig. 2.8). The main problem associated with the $SENB$ specimen is that the loading configuration is unstable for short cracks and inaccurate for long ones, thus making the relaxation tests inefficients. Moreover, a very stiff testing machine is needed. The DCB specimen has the advantage of a straight crack front (as opposed to the complicate curved front of the DT specimen). A major drawback, however, is that the K calibration is a function of the crack length, unless the compliances of the specimen and loading system are

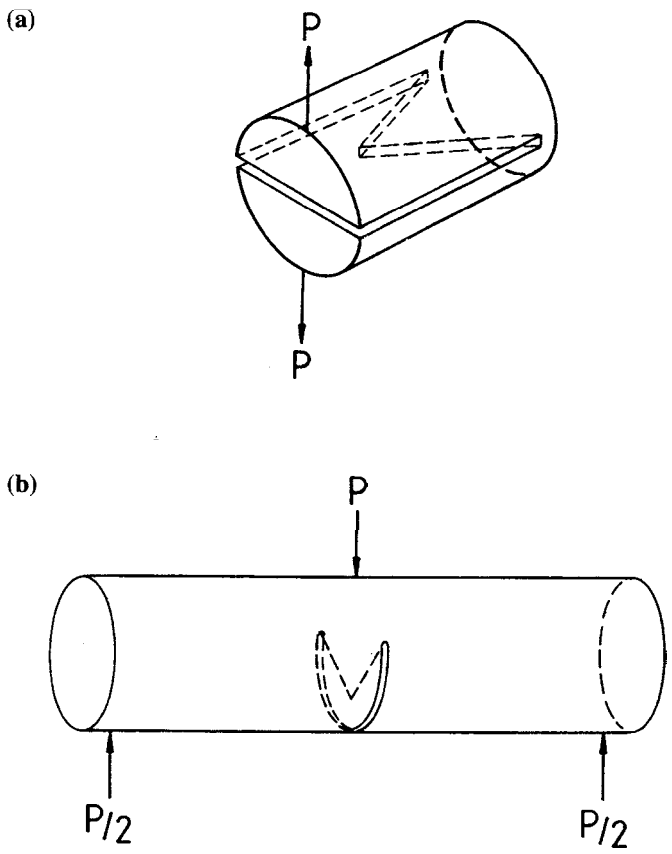

Figure 2.6: Schematic drawings of chevron-notched specimens. (a) Short-rod specimen. (b) Chevron-notched round bar in bending.

matched exactly. The suitability of chevron-notched specimens for studying subcritical crack growth is still being studied.

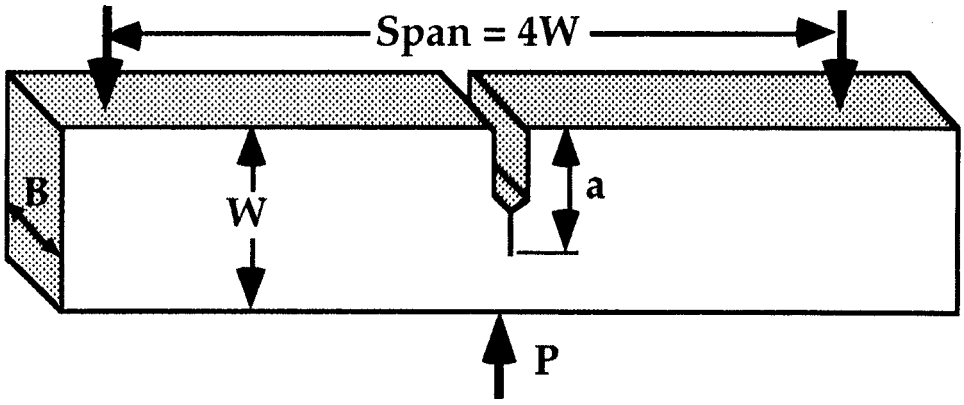

Figure 2.7: Singe Edge Notched Beam (*SENB*) in bending.

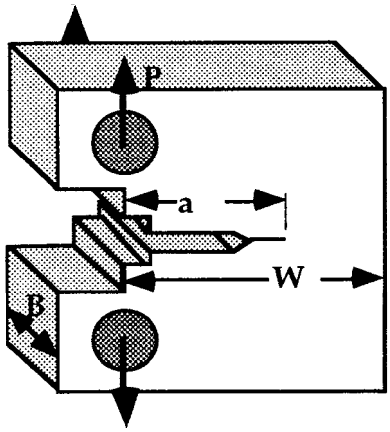

Figure 2.8: Double Cantilever Beam (*DCB*).

Chapter 3

The Double Torsion load relaxation method

3.1 The specimen geometry and loading configuration

The double-torsion load relaxation (constant displacement) method was developed by Evans [10] to obtain the velocity of crack propagation versus the mode I stress intensity factor (*SIF*).

A typical double-torsion specimen is shown in Fig. 3.1(a). A constant displacement is applied to the specimen through a four point bending scheme. A notch is machined at one end of the specimen to produce the initiation of the crack. A side groove performed on the bottom face assures the propagation of the crack front along the median plane of the specimen.

The advance of the crack has the effect of increasing the specimen compliance. Since a fixed displacement is imposed, this results in a progressive relaxation of the load. At the same time, the measurement of the load in time allows one to invert the evolution of the crack length.

The instant value of the *SIF* can be obtained directly from the load P. The value of the crack velocity can be obtained by the load relaxation rate. During a single test, the load is progressively relaxed, so that the whole characteristic curve can be obtained by putting into relation the values of K_I and v.

The method has various advantages, the main of which is its capability to produce stable crack propagation, which makes it very convenient for studying fracture in brittle materials like rocks [4]. Thanks to this stability, more tests are possible on the same specimen. Another advantage of the method is that it only requires one to monitor the decrease of the load with time to

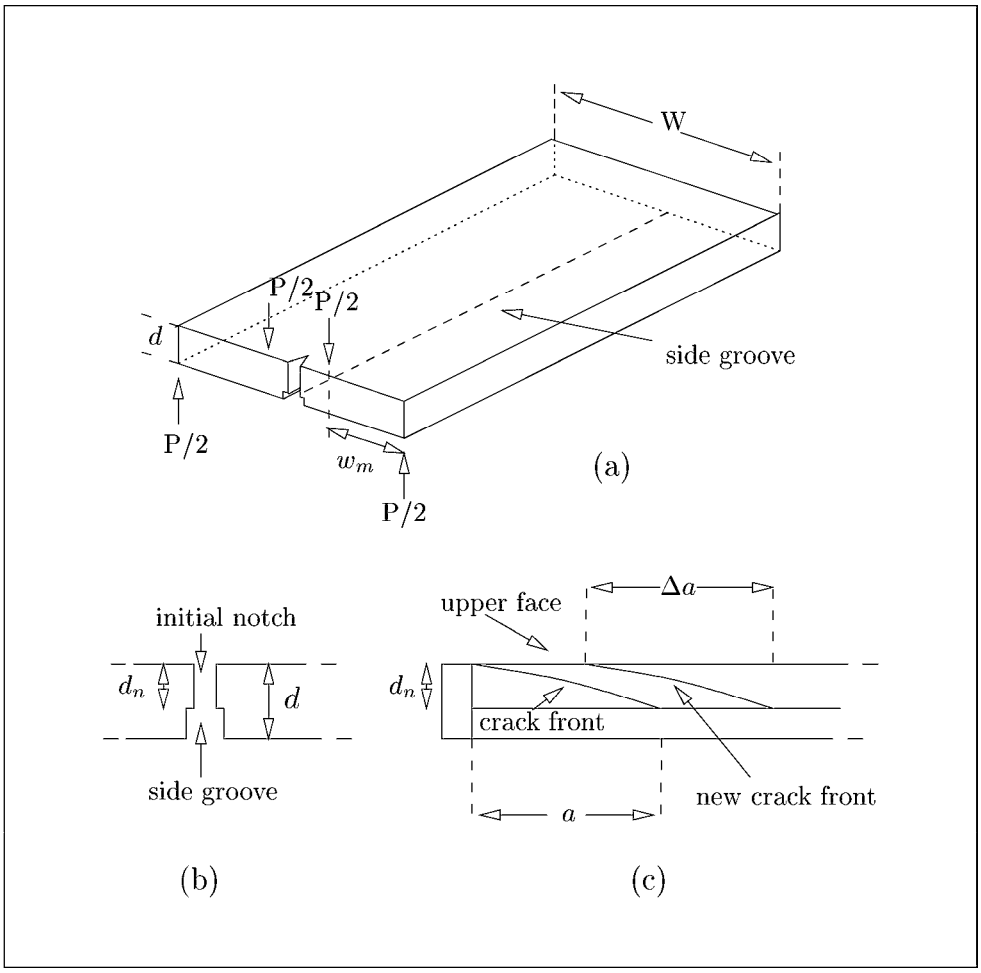

Figure 3.1: Sketch of a double torsion specimen: (a) general view, (b) axial cross section, (c) longitudinal cross-section (modified after Atkinson [2]).

measure both the stress intensity factor and the crack velocity, without any need to measure the crack length during the experiment.

3.2 Evans' model

The *DT* specimen can be considered as two elastic torsion bars, each having a rectangular cross-section and a length equal to the crack length a, loaded as indicated in Fig. 3.2 to a load of $P/2$. It has been shown [33] that for small deflections, y, the torsional strain angle, θ, is given by

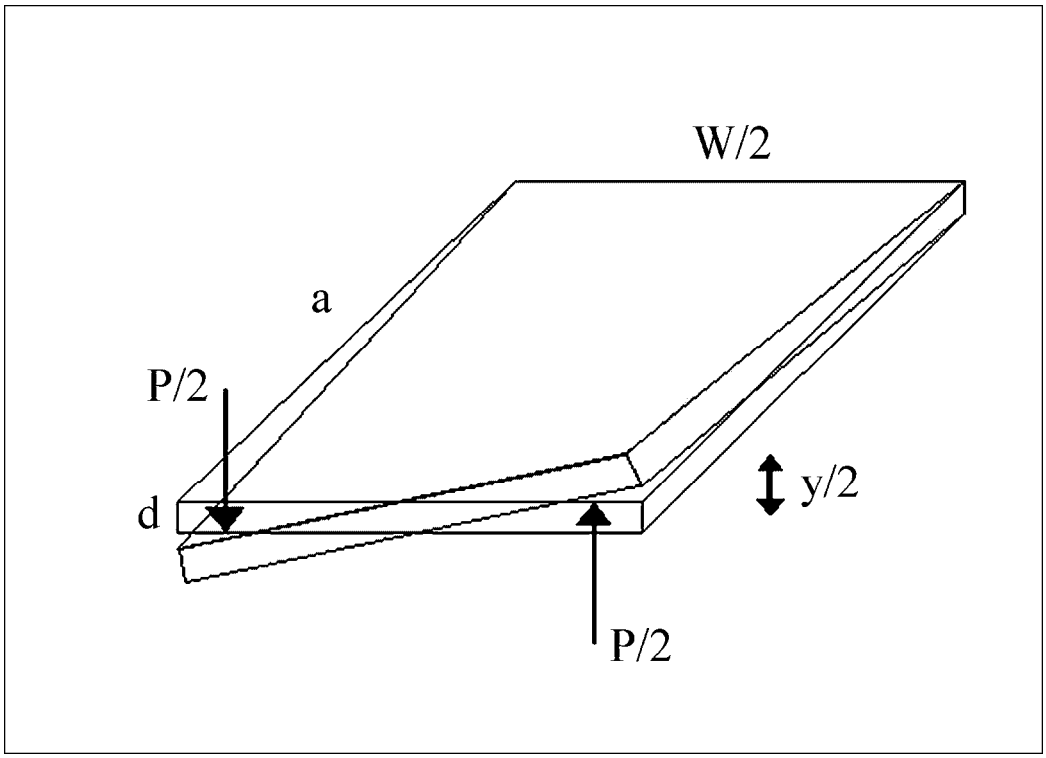

Figure 3.2: The *DT* specimen can be considered as two elastic torsion bars, each having a rectangular cross-section and a length equal to the crack length a.

$$\theta \approx y/w_m \approx \frac{aP}{\eta w_m W d^3 \mu} \tag{3.1}$$

where w_m is the moment arm of the torsion, W the specimen width, d the specimen thickness, μ the shear modulus, and $\eta = 1/3$ for $W \gg d$ (thin specimens). As W/d decreases, η decreases as described by Timoshenko [33].

The specimen elastic compliance, C, is then given by

$$C = \frac{y}{P} = \frac{w_m^2 a}{\eta W d^3 \mu} \tag{3.2}$$

The strain energy release rate for crack extension, G, is related to the specimen compliance by the expression [14]

$$G = -\left(\frac{dU}{dA}\right) = \frac{P^2}{2}\frac{dC}{dA} \tag{3.3}$$

where U is the elastic strain energy, and A is the area of the crack. If

the shape of the crack front is independent of crack length (see § 5.2.4) then $dA = d_n da$, where d_n is the thickness in the plane of the crack. By differentiating Eq. (3.2) with respect to a and substituting into Eq. (3.3) we obtain

$$G = \frac{P^2}{2d_n}\frac{dC}{da} = \frac{w_m^2 P^2}{2\eta W d^3 d_n \mu} \tag{3.4}$$

3.3 Stress intensity factor and crack velocity

For plane stress, the mode I stress intensity factor, K_I, is related to G by

$$K_I = \sqrt{EG} = P w_m \sqrt{\frac{E}{2W d^3 d_n \mu}} \tag{3.5}$$

Since the Young's modulus E and the shear modulus μ are related by

$$\mu = \frac{E}{2(1+\nu)} \tag{3.6}$$

where ν is the Poisson's ratio, Eq. (3.5) reduces to

$$K_I = P w_m \sqrt{\frac{(1+\nu)}{\eta W d^3 d_n}} \tag{3.7}$$

The *SIF* is thus a function of the applied load, specimen dimensions, and Poisson's ratio only. It's independence of the crack length makes the *DT* specimen extremely useful.

Since this model is based on the assumption that the specimen can be treated as two independent torsion bars, and therefore that the uncracked portion of the specimen remains substantially undeformed, the validity of these equation is limited to relatively large crack lengths. The validity of the model was tested experimentally by Williams and Evans [36] performing a compliance calibration on a specimen and comparing the empirical relationship with that which would result from the analytical expression (Eq. (3.2)). Figure 3.3 shows a set of experimental compliance data for a steel specimen with the dimensions indicated. The data fits very well a linear relation

$$C = y/P = Ba + D \tag{3.8}$$

but the intercept D is generally different from zero, probably due to the end effect of short crack lengths. Differentiating Eq. (3.8) as a function of time at constant displacement gives

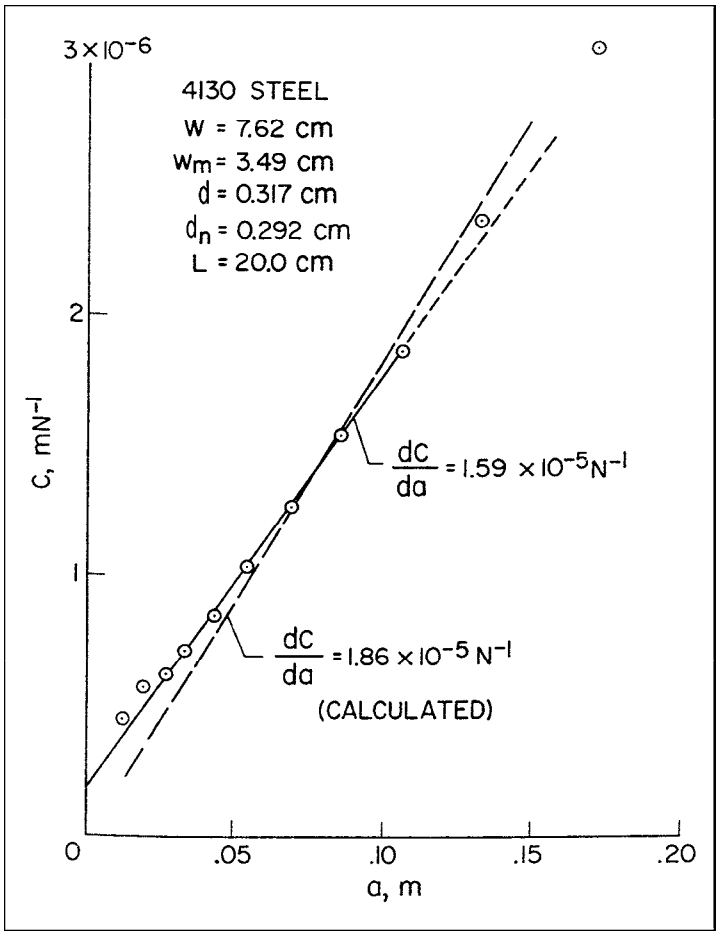

Figure 3.3: Experimental compliance calibration on steel specimens (modified after [36]).

$$\left(\frac{da}{dt}\right)_y = -\frac{Ba + D}{BP}\left(\frac{dP}{dt}\right)_y \tag{3.9}$$

From Eq. (3.8) it can be seen that, for constant displacement

$$P(Ba + D) = P_i(Ba_i + D) = P_f(Ba_f + D) \tag{3.10}$$

where P_i and a_i are the initial values of load and crack length, and P_f and a_f are the corresponding values at the completion of relaxation. Solving for $(Ba + D)$ and substituting in Eq. (3.9) gives

$$\left(\frac{da}{dt}\right)_y = -\frac{P_{i,f}}{P^2}[a_{i,f} + D/B]\left(\frac{dP}{dt}\right)_y \tag{3.11}$$

In general, except for very low modulus materials (such as polymers) or for small crack length, $D/B \ll a_i$, so that

$$\left(\frac{da}{dt}\right)_y = -\frac{P_{i,f}a_{i,f}}{P^2}\left(\frac{dP}{dt}\right)_y \tag{3.12}$$

The crack growth rate at each load can thus be found from the rate of load relaxation, if the crack length at the onset or completion of relaxation is also measured.

3.3.1 Inclination of the crack front

It should be noted that the crack front is not flat for this type of specimen (see Fig. 3.1(c)), so that the crack has a different extension on the two faces of the specimen. The term "crack length" used herein refers to the longest portion of the crack, that is, the length at the lower (opening) face of the specimen. Moreover, the length of the crack is measured starting from the position of the loading points.

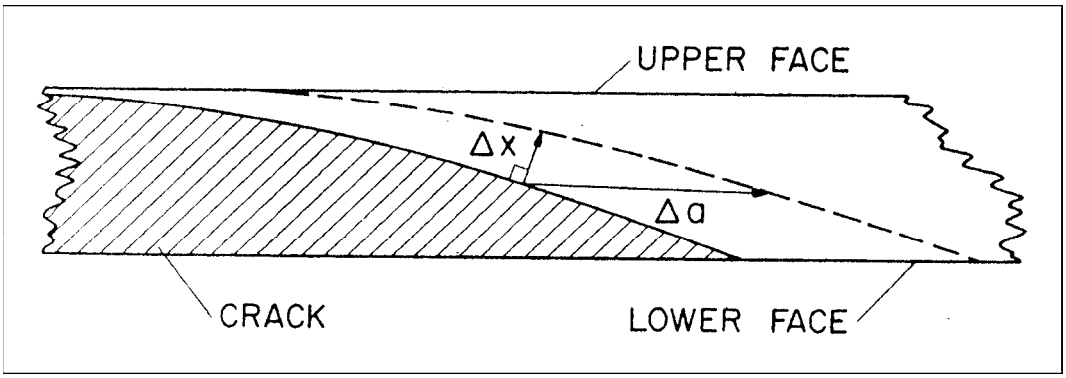

Figure 3.4: The effective direction of propagation of the crack is normal to its front.

The difference Δa in crack extension between the upper and lower faces of the specimen has been empirically found to be fixed and equal to five times the thickness d_n in the plane of the crack for glass and alumina [10].

The effective direction of propagation of the crack is normal to its front. The inclination of the crack front implies that the crack velocity is not given directly by da/dt (see Fig. 3.4), but it should be reduced about a factor ϕ [10] approximately given by

$$\phi \approx d_n/\sqrt{\Delta a^2 + d_n^2} \tag{3.13}$$

The crack velocity v is then given by

$$v = -\phi a_{i,f} P_{i,f} \frac{1}{P^2} \frac{dP}{dt} \tag{3.14}$$

Chapter 4

Experiments on lava rocks

4.1 Test material

Our specimens were cut from samples of volcanic rocks extracted from the Mount Etna, Sicily, 1981 flank eruption, from the Punta dello Scoglitto lava flow, from the Fossa latitic eruption, from the Lentia rhyolitic dome, all at Vulcano, Aeolian Islands, and from the shoshonitic basaltic eruption at the Filo del Fuoco in Stromboli, Aeolian Islands. The rocks from Vulcano and Stromboli are all dated between 113,000 years b.p. and the historical epoch (Calanchi *et al.* [5]). Petrographic analysis shows a homogeneous vesicular porphyritic structure in most of the samples, allowing us to assume isotropic mechanical properties. The porosity is determined by sub-spherical pores of variable dimensions ranging from fractions of a mm to a few mm. The chemical composition of each type of rock is determined by XRF analysis; the percentages of the main oxides are reported in Table 4.1. The lithotypes are displayed on a TAS diagram (Total-Alkali-Silica) in Fig. 4.1.

4.2 Optimizing the experimental technique

We attempted to achieve a better accuracy in measuring the fracture parameters by optimizing several experimental aspects. These were

- A very sturdy machine, run at a small fraction of its load capability.
- Careful specimen preparation, which included low tolerance machining.
- Tight control of the experimental conditions (temperature and humidity).

Spec.	SiO_2 %	TiO_2 %	Al_2O_3 %	Fe_2O_3 %	MnO %	MgO %	CaO %	Na_2O %	K_2O %	P_2O_5 %	LOI %
V1	54.13	0.60	17.22	8.12	0.16	3.20	7.20	5.14	3.73	0.49	0.79
V2	59.71	0.47	17.42	6.13	0.13	1.87	4.54	4.17	5.03	0.33	5.29
V3	70.74	0.22	14.21	3.32	0.08	0.66	2.15	3.87	4.62	0.11	0.53
V4	58.19	0.60	18.72	7.06	0.11	1.37	3.70	4.05	5.74	0.46	1.59
S1	51.11	0.86	18.49	8.64	0.17	4.81	10.51	2.82	2.17	0.42	0.1
E1	47.88	1.58	17.74	3.29	0.19	4.73	10.36	4.69	1.53	0.42	0.75

Table 4.1: Percentage of major oxides in the specimens (from XRF analysis) normalized to 100 and LOI percentage (Lost Oxides Index). The content of FeO was zero for all rocks except E1, for which it was 6.83 %. The different lithotypes analyzed are relative to the Mount Etna, Sicily, 1981 flank eruption (E1), to the Punta dello Scoglitto lava flow (V1), to the Fossa latitic eruption (V2 and V4), to the Lentia rhyolitic dome (V3), all at Vulcano, Aeolian Islands, and to the shoshonitic basaltic rocks at the Filo del Fuoco in Stromboli (S1), Aeolian Islands. The rocks from Vulcano and Stromboli are all dated between 113,000 years b.p. and the historical epoch.

- High resolution digital electronics and data processing, which also allowed an improved accuracy in the measured elastic parameters.
- An optical check of the prefracture length.

4.2.1 The loading machine

The machine we used to apply the load is functionally similar to the widely used Instron testing machine and consists essentially of a servo-controlled electric motor which, through a cascade of worm gears, can apply a given displacement to a specimen, while measuring the applied load by a load cell mounted in series with the specimen. Our machine (see Fig. 4.2) is custom designed and built to maximize stiffness, with a solid stainless steel frame 25.4 mm thick. It was designed for a nominal working load of 20000 N and, to further guard against frame deformation, it was always used at loads less than 1500 N. Specimens may be up to 20 mm thick and up to 200 mm wide.

4.2.2 Specimen preparation

Specimens for double torsion testing were machined using a precision diamond head into slabs about 200 mm long, 70 mm wide, and with a set of

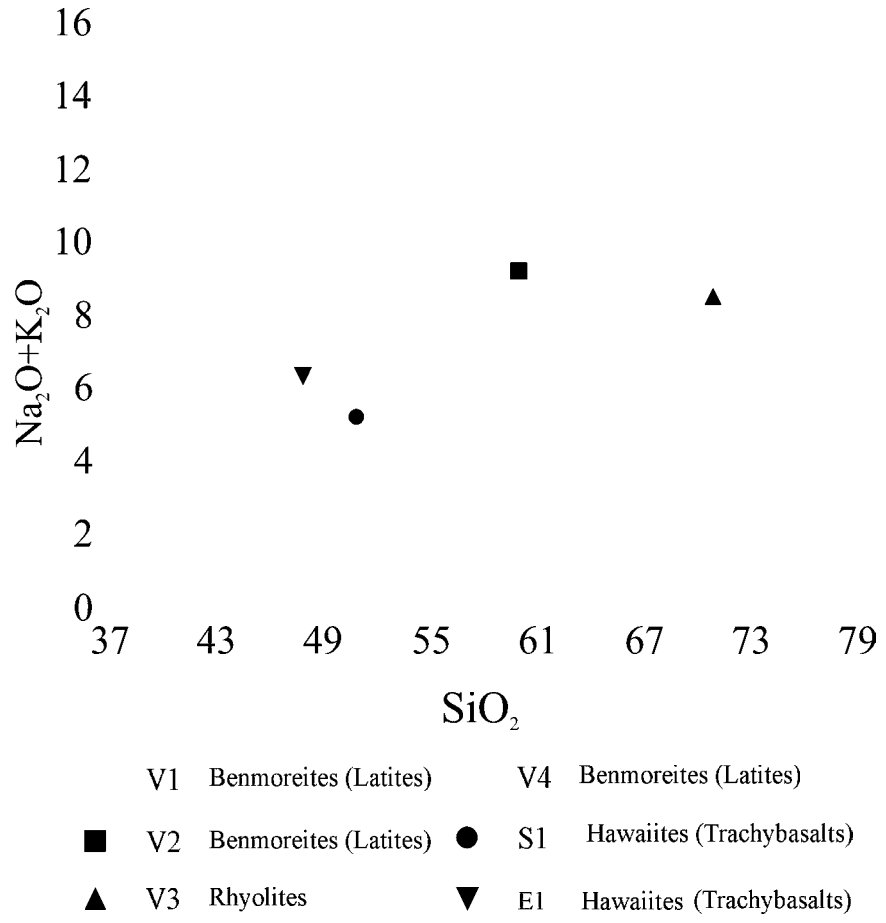

Figure 4.1: TAS diagram (Total-Alkali-Silica) for all the lithotypes analyzed.

Figure 4.2: A photograph of the loading machine.

different thickness values ranging between 4.7 mm and 9.4 mm. A 1 mm wide groove with a depth equal to 1/3 the specimen thickness was also machined along one of the faces along with a 10 mm long, 1 mm wide edge notch to guarantee a rectilinear propagation of the fractures. The tolerance was always kept within 0.4 mm. We used width to thickness ratios between 8:1 and 15:1, at which Eq. (3.7) is well applicable with the use of the appropriate values for η (see § 5.2.1).

4.2.3 Control of the experimental conditions

Since tiny deformations in the frame of a stiff loading machine can greatly affect the applied load, it is essential that temperature be kept as constant as possible. We used a heat pump and an electronic differential thermostat to keep temperature variations within $1°C$ in a dedicated room. The variations of humidity, which does not affect the loading machine, but which can affect the fracture properties of the rock, were kept within 10 %.

4.2.4 High resolution electronics

The high resolution achievable through up-to-date electronic devices was beneficial to two different experimental steps. First, the output of the load cell was fed into an analog–digital converter, digitally amplified, and sent via a serial port to a computer workstation where it was recorded, to guarantee the acquisition of massive data sets. Second, since Eq. (3.7) requires the knowledge of the Poisson's ratio ν, we developed a procedure that used isotropic elastic wave velocities to measure ν:

$$\nu = \frac{[(\frac{V_p}{V_s})^2 - 2]}{2[(\frac{V_p}{V_s})^2 - 1]} \tag{4.1}$$

Essentially, we used the standard time-of-flight measurement for pulse trains of P and S waves between a sensor and an emitter placed at given positions on the specimen. Step functions with exponential fall were generated by a function generator, pulsed at frequencies varying from 10 Hz to 1 kHz, and injected into the specimen as elastic waves by means of a custom-built piezoelectric transducer, checking in all cases that the frequency value was far from the resonance of the specimen. Time stacking of the recorded signal was then used together with an averaging over 1000 pulses. This allowed an improvement in the signal to noise ratio of approximately 20 db.

For each specimen the wave velocities were calculated twice for seven different configurations of the transmitter and receiver, which were glued to

Specimen	$V_p(km/s)$ $I_q - III_q$	$V_s(km/s)$ $I_q - III_q$	ν	K_{Ic} $(MNm^{-3/2})$
V1	1.44 – 1.78	0.88 – 1.04	0.24	0.445
V2	3.05 – 3.16	1.80 – 2.13	0.17	1.006
V3	3.48 – 3.62	1.92 – 2.26	0.24	1.248
V4	2.30 – 2.53	1.26 – 1.69	0.26	0.165
S1	1.86 – 2.06	1.21 – 1.39	0.11	0.227
E1	3.31 – 3.43	1.89 – 2.15	0.21	1.763

Table 4.2: The scatter in the P and S wave velocities in each specimen for all directions of propagation is given by the I and III quartile values. The median value of the Poisson's ratio ν is given in the third column. The last column shows the corresponding fracture toughness K_{Ic} value. The different lithotypes are given in the caption of Table 4.1.

the specimen by using cyanoacrilate compounds to ensure good mechanical coupling. The internal scatter of each P and S wave velocity measurement was within a few percent, and also the variation for the different travel paths was limited to about 10 % for P waves and 20 % for S waves. This indicated a fairly modest anisotropy, which made it possible to apply the isotropic approximation, implemented by taking the median value for each sample. The scatter on the measurements is given by the I and III quartile values of the velocities measured in all directions, which are shown in Table 4.2 along with the median Poisson's ratio. A detailed report of the measures can be found in the graduate thesis of Nicola Negri [21] and Lorena Sassi [29].

4.2.5 Optical check of the prefracture length

In order to employ equations (3.7) and (3.14) it is necessary to create an initial fracture of known length in the specimen. The traditional approach consists, first of all, of cutting a notch of given length along its major axis (see Fig. 3.1a, 3.1b). Since this cut will have a blunt end, while it is necessary to have a sharp fracture, the specimen is loaded at the lowest possible constant strain rate and the load is closely monitored. As soon as a decrease in load is observed, loading is immediately stopped. A typical prefracture load–versus–time curve is shown in Fig. 4.3. It clearly shows the loading at constant rate, followed by a knee. The drop in load is interpreted as the initiation of a fracture, which is nevertheless classically assumed to have propagated for such a short length that it can be disregarded. In light of this, the length of the initial fracture is classically taken to be that of the notch. We checked

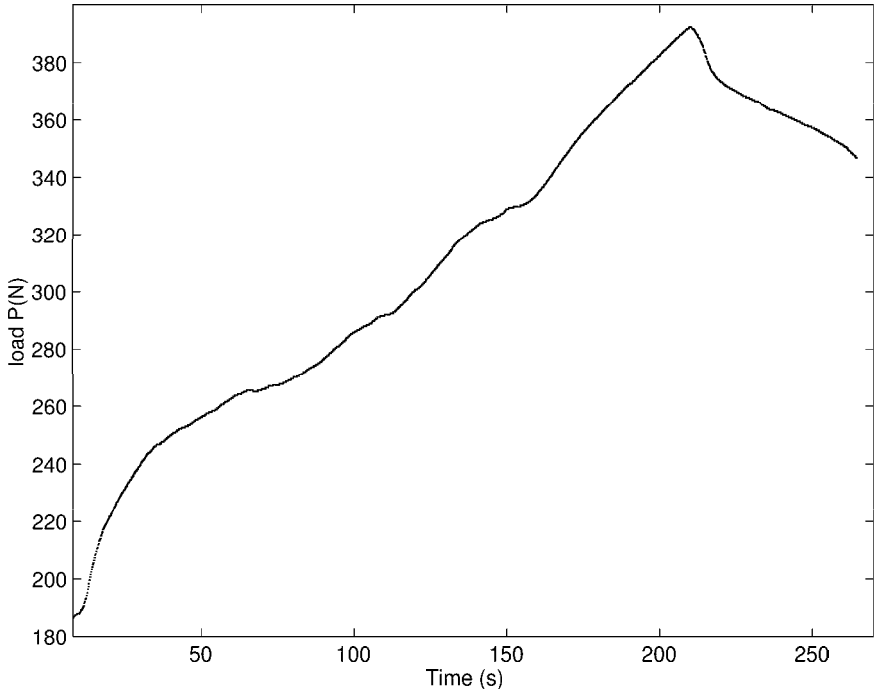

Figure 4.3: The load curve in a typical pre-fracture run. The fracture is initiated at ≈220 seconds when a load drop occurs.

this by observing the presence of a fracture in the groove (opening side) with an optical stereo microscope. We have in most cases found that a fracture can be quite easily observed and that its length (generally a few centimeters) can never be disregarded. In general, we were also able to observe the final length of the fracture after a relaxation run and this value was cross-checked with the initial one using the constant displacement condition (Eq. 3.10).

The apparatus proved to be very stable so that several relaxation runs could sometimes be performed on the same specimen.

4.2.6 Determination of fracture toughness K_{Ic}

All the measurements of the critical load P_c were performed on pre–fractured specimens. One or more specimens for each lithotype were loaded at the highest possible rate until they broke and the relative K_{Ic} was then calculated through Eq. (3.7) (the median value for each lithotype is reported in Table 4.2). The loading curves have a general aspect as in Fig. 4.4,

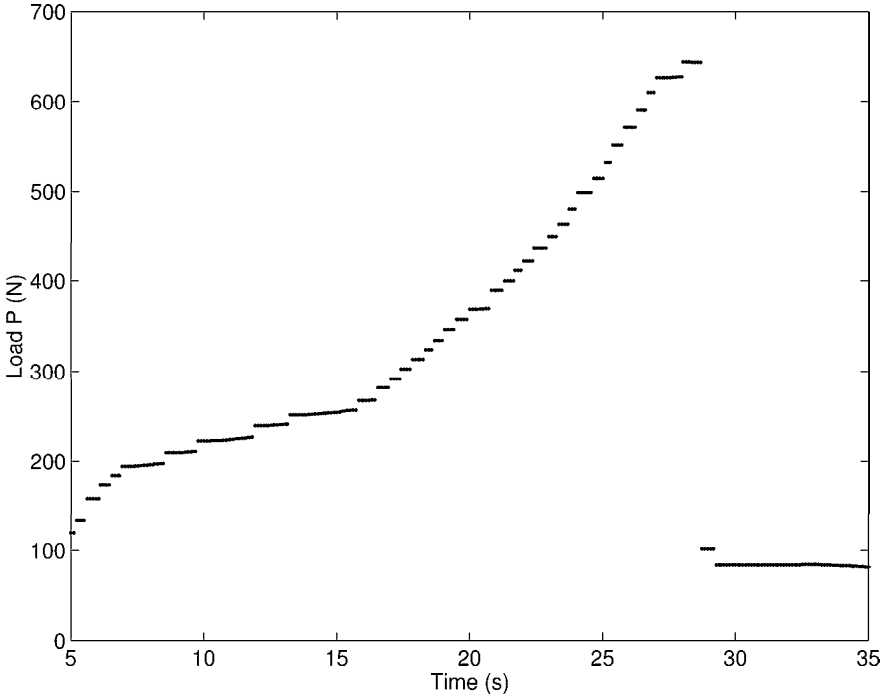

Figure 4.4: The general aspect of a critical loading curve consists of a sharp rise of the load followed by an instant drop consequent to the specimen failure.

showing that no significant relaxation takes place before the failure. At this point the load relaxation procedure was ready to start.

4.2.7 Load relaxation tests

A specimen was loaded at the highest possible rate up to 90–95 % of the load relative to K_{Ic}, the machine was stopped and the load relaxation with time was recorded.

Load was sampled at 10 Hz for the whole run, which typically lasted 10 hours. Only the initial part of load relaxation was actually used ($\simeq$ 1000 s), though, due to the load fluctuations induced by temperature in spite of its tight control, which are apparent when the relaxation rate becomes slow (see Fig. 4.5 and the discussion below).

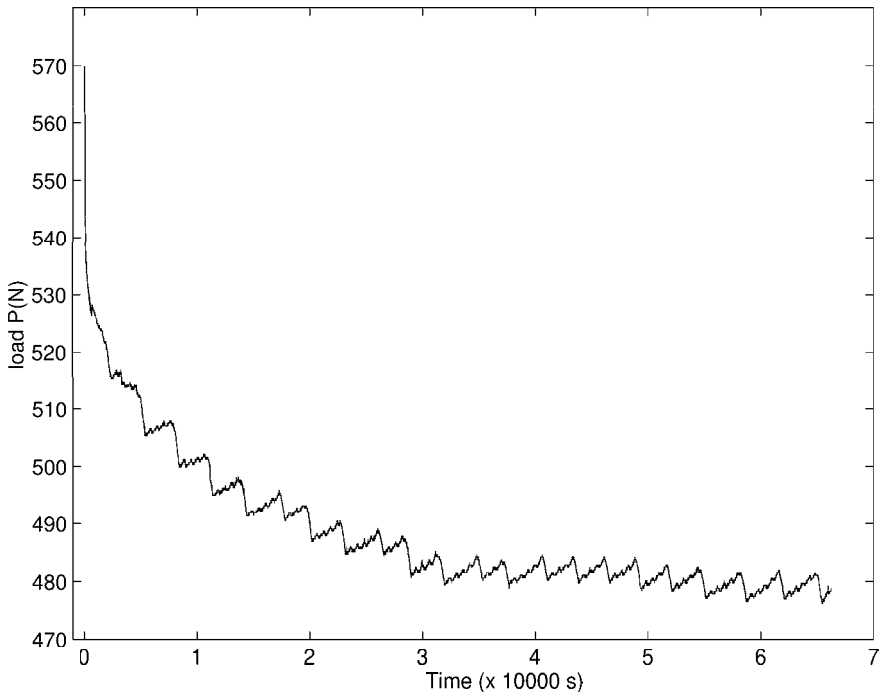

Figure 4.5: A typical load relaxation curve. The load fluctuations induced by periodic temperature variations are clearly apparent.

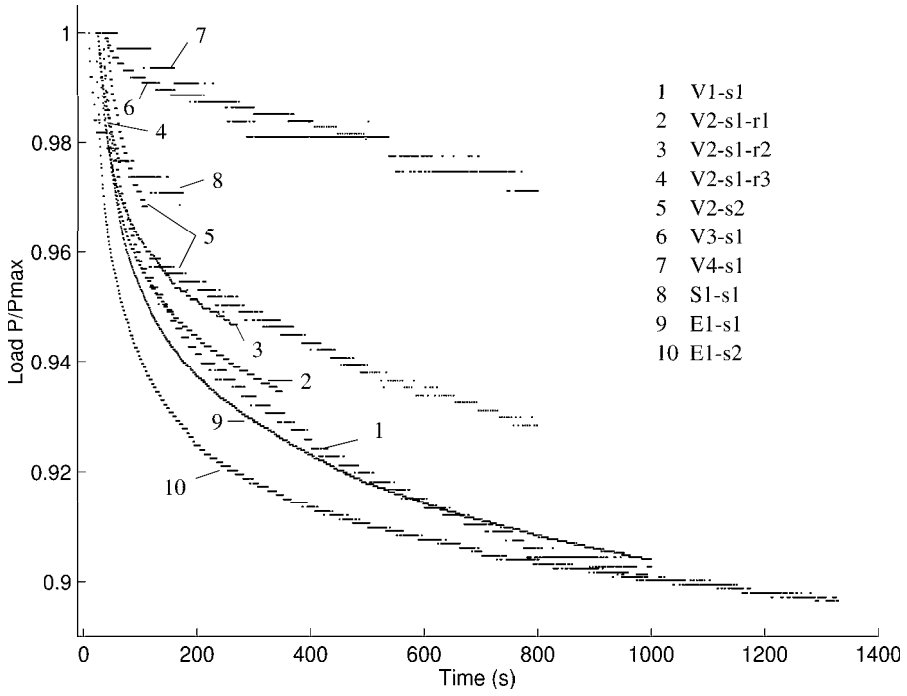

Figure 4.6: The initial part of the load relaxation curves, which were used in the analysis, each one normalized to the maximum load Pmax reached in the run. The label numbers are the same as in Table 4.3.

4.3 Results

Sixty-five specimens were cut from a total of 70 kg of lava rocks. A fraction of them had to be discarded because they contained void inclusions large enough to prevent effective measurements. Another fraction accidentally broke during the machining. A further fraction had to be discarded for an insufficient number of samples of identical lithotype.

We measured 6 different lithotypes, respectively one coming from Mount Etna volcano, four from Vulcano and one from Stromboli. In spite of the tight control of the environment conditions, the load fluctuation induced by the near periodical temperature variation due to the thermoregulation cycle was generally large (see Fig. 4.5). We could thus only measure the initial part of the relaxation curve, in which the relaxation rates are high and the load fluctuations induced by temperature variations are comparatively small. Each relaxation curve was therefore analyzed only in the interval

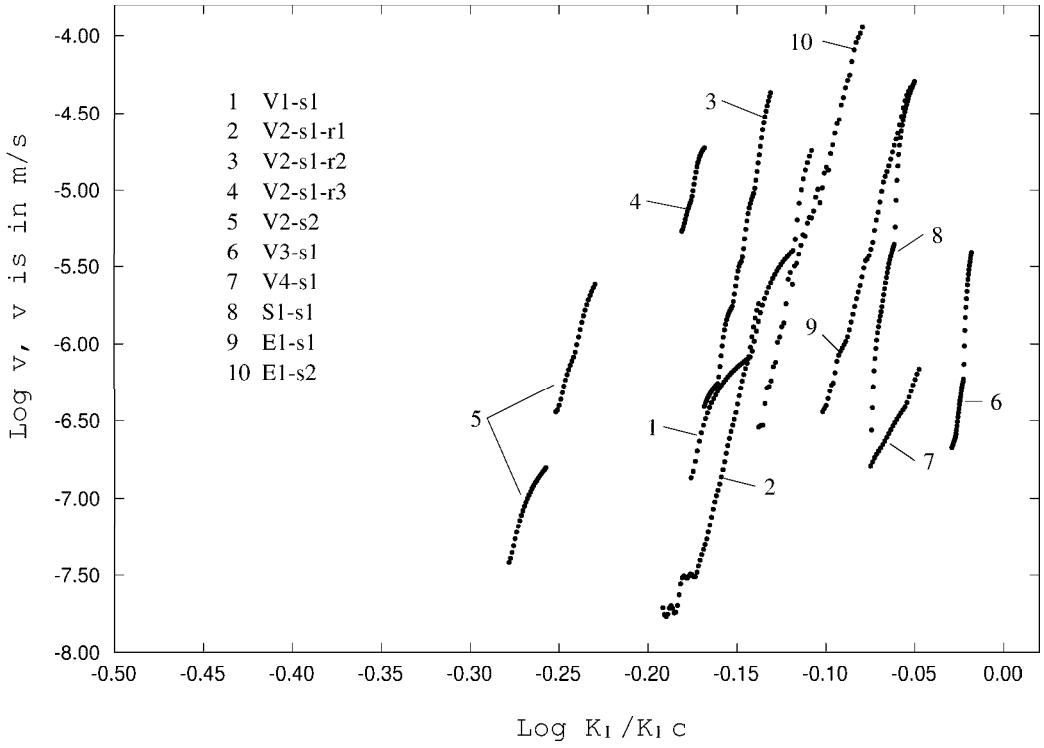

Figure 4.7: Region III of the subcritical crack growth curves ($K_I - v$). The stress intensity factor is normalized to the critical value of each lithotype. Notice the coherence and linearity in the slope. The horizontal separation is due to the different values of K_Ic and is related to the different lithotypes.

preceding the first evident effect of temperature fluctuations (Fig. 4.6). As a consequence, we could not measure the whole subcritical $K_I - v$ curve relative to mode I fracture propagation, but only its region III, which regards the highest velocities of propagation. This is actually the most important one for modeling purposes, since it immediately precedes catastrophic propagation. The dependence of v on K_I in region III is well approximated by a power law:

$$v = AK_I^n \tag{4.2}$$

where A is a constant and n is the subcritical crack growth index. The experimental results are reported in Fig. 4.7.

The measured velocities of propagation were in the range 10^{-7} to 10^{-4} m/s, in which a log-linear relation was found to provide a very good fit to the data ($r^2 \geq 0.90$ in all cases). Since theoretical considerations yield that these slopes remain constant up to the critical value of the stress intensity

	Specimen	n
1	V1-s1	25.4
2	V2-s1-r1	49.3
3	V2-s1-r2	61.5
4	V2-s1-r3	47.2
5	V2-s2	36.5
6	V3-s1	125
7	V4-s1	22.6
8	S1-s1	92.1
9	E1-s1	43.1
10	E1-s2	45.9

Table 4.3: The experimental log exponents of the velocity of fracture propagation versus stress intensity factors in the region III of the mode I subcritical fracture propagation, for the lithotypes we considered. The different lithotypes are given in the caption of Table 4.1. Letter 's' denote different specimens of the same lithotype. Letter 'r' denote different relaxation tests on the same specimen.

factor [4], it is possible to calculate the evolution of fracture propagation from velocities of 10^{-7} m/s to catastrophic propagation. The values of the subcritical fracture propagation index n for each lithotype are given in Table 4.3. Particularly important is the case of the Etna (E1) and Vulcano (V2) lithotypes, for which several independent relaxation runs could be performed, respectively 2 for E1 and 4 for V2. A good coherence was found, with repeatability of the measurement of the region III fracture slope within 20%.

Chapter 5

Critical analysis of Evans' model

5.1 Variability in the estimates

Although the Double-Torsion load relaxation method has been almost the sole method used to study subcritical cracking in the last thirty years, the measurements of the $K_I - v$ curves are unavoidably marred by considerable scatter [3], [32].

Swanson [32] has shown that for a given specimen geometry values of the stress corrosion index n are repeatable to a degree, but that there exist rather large differences in the mean values of n determined for the same material in different laboratories. These differences can not be attributed to variations in the material. Furthermore, the placement of the $K_I - v$ curves on the stress-intensity axis is not fully repeatable using the load relaxation method, i.e., there is a low precision in the preexponential constant in Eq. (2.15).

Some reasons for this variability are the heterogeneity of the rock samples, the sensitivity to environmental conditions, and the difficulty and cost of preparing specimens with low geometrical tolerances.

There has been a considerable recent discussion in the literature regarding the constraints on the validity of the double torsion method. Various factors have been identified as possible sources of errors and uncertainties in DT data, and assumptions of the method have been found not to be satisfied in certain specimen geometries. The following sections report the main observations and conclusions on this subject. Some progress has been made in the comprehension of the limitations of the DT method. Nevertheless much remains to be understood before the DT method can be assumed as an accurate standard for studying subcritical cracking.

W/d	r	t	η	3η
2	1	1	0.1406	0.4217
8/3	4/3	3/4	0.1805	0.5414
4	2	1/2	0.2287	0.6860
6	3	1/3	0.2633	0.7900
8	4	1/4	0.2808	0.8424
10	5	1/5	0.2913	0.8740
12	6	1/6	0.2983	0.8950
16	8	1/8	0.3071	0.9212
24	12	1/12	0.3158	0.9475
40	20	1/20	0.3228	0.9685

Table 5.1: Corrective factors η for a finite thickness DT specimen as a function of the thickness ratio, which is sometimes indicated as $r = W/2d$ or $t = 2d/W$.

5.2 Known drawbacks of Evans' formulation

Let us recall here the basic hypothesis that lay below the classical Evans' model: the DT specimen is considered as a symmetrical system of two independent thin plates, each of which subjected to simple torsion, with length equal to the crack length. The part of the specimen beyond the fracture tip is considered undeformed. The compression induced by torsion at the contact zone of the two plates on the upper face (see Fig. 3.1) is ignored. Moreover, the presence of the side groove, the effect of its shape, and the presence of the initial notch are ignored as well. Finally, the effect of the inclination of the crack front is only taken into account for what concerns the crack velocity, but not for the strain energy release rate.

5.2.1 Thick specimens

In Eqs. 3.1 to 3.7, Evans [10] assumed the use of $\eta = 1/3$ in the limit of thin specimens ($W/d > 12$). The original equation for the simple torsion of a plate with a finite thickness was derived analytically by Timoshenko [33], and its transfer to the DT specimen was reviewed by Fuller [12]. The factor η was given as a tabled function of the thickness ratio W/d (see Table 5.1).

For $W > 2d$ (that is, a square beam cross section), a simplified expression which is accurate to better than 0.1% was provided by Fuller [12]

$$\eta \approx \frac{1}{3} - 0.2101t + 0.4te^{-\pi/t} \tag{5.1}$$

For independent beams in torsion, Eq. (3.2) is an exact expression for the compliance with the correction for finite thickness beams given by the coefficient $\eta(t)$. For the *DT* configuration, however, the contact stresses resulting from the overlap of the two beams depend on the beam thickness. Accordingly, the correction for finite thickness given by Eq. (5.1) may not be the most important correction for thicker specimens [12].

Some experimental tests performed by Evans [11] showed that use of Eq. (3.7) with the proper value of η, underestimated K_{Ic} for specimens with a thickness ratio of $t \sim 1/4$, but was in agreement with other measurements of K_{Ic} when t was higher then $1/6$ ($W/d > 12$). It is probably due to this effect that Evans decided to use thin specimens.

5.2.2 Plane-strain vs. plane-stress

Eq. (3.7) was obtained under plane-stress assumptions, but the effective deformation condition at the neighboring of the crack is unknown, since the crack profile is curved and three-dimensional. Some authors assume plane-strain conditions [26], so that the mode I *SIF* would be:

$$K_I = P w_m \sqrt{\frac{1}{\eta(1-\nu) W d^3 d_n}} \tag{5.2}$$

When the process zone size is small compared with the specimen thickness or z dimension (Fig. 2.2) the crack stress field in the central portion of the crack front is nearly plane-strain because of the constraining effect of the crack tip. If the z direction or specimen thickness is small compared to the non-linear zone, then the plane-strain constraint of the crack tip zone is also small and plane-stress analysis is more appropriate [4].

If the minimum thickness of $2.5(K_{Ic}/\sigma_y)^2$, where σ_y is the yield strength, that is recommended by the ASTM Test for Plane-Strain Fracture Toughness in Metallic Materials (E399), is appropriate for these brittle materials, then most measured values have probably been plane-strain fracture toughness [12]. The choice between these two assumptions remains an open question, and may not even be an appropriate question to ask.

5.2.3 Crack tip displacement mode

Another objection that has frequently been raised about the *DT* configuration is the appropriateness of describing the mode of failure as mode I [12]. However, this can be the only mode of crack deformation in an "ideal" *DT* specimen, since the loading configuration and the specimen geometry are symmetrical about the crack plane. In support of this proposition Evans and

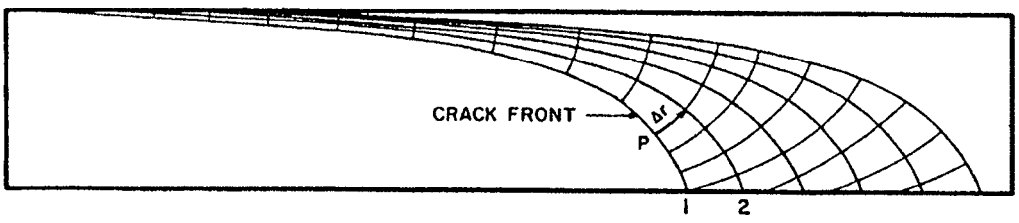

Figure 5.1: Successive positions of the crack front in DT specimen during subcritical crack propagation. Velocity at P is given by $v(P) = lim_{\Delta t \to 0} \Delta r(P)/\Delta t$.

co-workers [10], [36] observe that measured values of K_{Ic} appear to agree with mode I values as given by Eq. (3.7), although they indicate that this could be a consequence of the relatively large values of K_{IIc} and K_{IIIc} compared to K_{Ic} for most materials.

5.2.4 Crack front shape

As it was observed in many previous studies on subcritical crack growth, the crack front in a DT specimen is curved (see Fig. 3.1) [10], [36]. It has also been reported that the shape of the crack front is independent of crack length (i.e. remains unaltered during crack propagation) for a constant stress-intensity factor and that the shape is different for different materials.

Virkar and Gordon [35] have shown that the shape of the crack front profile is dependent on the characteristics of subcritical crack growth in any given material in any given environment.

Let us consider successive positions of the curved crack front, as in Fig. 5.1. Since the local direction of crack propagation is orthogonal to the crack front, it is readily apparent that the crack velocity v varies all along the crack front, the highest velocities being at the lower face.

Since v is related to K via a relation in the form $v = AK^n$, this implies that K is also a function of the position along the crack front. Since the stress-corrosion index n is generally large for brittle rocks, small variations in K produce large variations in v. The crack front shape was shown to depend on the value of n [35], so that the crack profile will meet the upper face more gradually in materials exhibiting large n values.

As a consequence, if the plot of v vs. K is not linear on a log-log scale, i.e. n is not constant, the shape of the crack front will continuously change during a load relaxation test, making the average estimation of v inaccurate.

This problem was addressed by Pollet and Burns [27] who derived a better

averaging process for the crack velocity along the front.

The experimentally measured quantities during DT testing are the apparent crack velocity, $\dot{a}$, and the average strain energy release rate, $G_{av}(\dot{a})$, obtained from a global strain energy analysis.

If we assume that, at least over a range of crack velocities encompassing those experienced by the crack elements, the $v(G)$ relation can be described by

$$v = v_0(G - G_0)^n \tag{5.3}$$

it can be demonstrated that the average value of G, G_{av}, is related to the apparent crack velocity by

$$\dot{a} = \left(\frac{v_0}{\phi}\right)(G_{av} - G_0)^n \tag{5.4}$$

where the coefficient ϕ is given by

$$\phi = \left(\frac{1}{d_n}\int_0^{d_n} sin\alpha(x,\dot{a})^{1/n}dx\right)^n \tag{5.5}$$

Pollet and Burns observed that crack profiles, and consequently ϕ, were almost independent of $\dot{a}$ in polymetil metacrylate (PMMA). Equation (5.4) has the same form of Eq. (5.3), with the same constant G_0 and same exponent n. Consequently, with the preceding restrictions DT data provides the correct value of the stress-corrosion index n. Comparing Eqs. (5.4) and (5.3) then provides the relation

$$v(G) = \phi\dot{a}(G_{av}) \tag{5.6}$$

that is, the same as in Evans' method, but with a new determination of ϕ. When the crack-front geometry is approximated by a straight line, $sin\alpha(x,\dot{a})$ is a constant, and $\phi = sin\alpha_0$ is then equal to the first-order geometrical correction proposed by Evans [10].

Moreover, Pollet and Burns showed that ϕ does not vary significantly with n, for $n > 4$. Thus ϕ can be accurately obtained even if n is not known precisely.

5.2.5 Side groove

The presence of the side groove is intended to guide the crack propagation along a straight line in the midplane, thus allowing the suppression of the effects from inaccurate dimensioning or inhomogeneities in the structure.

However, the presence of the groove is not accounted for in Evans' model for the specimen deformation, whereas the width and the depth of the groove and the shape of its tip could influence the determination of K_I.

To investigate on the effect of the groove, some DT tests were performed by Pabst and Weick [25] on commercial Al_2O_3 material using the constant load technique. The main results are that the presence of a groove introduces a substantial scatter in the estimates of the stress corrosion index n. Such a scatter was larger for the larger groove with a square shaped geometry than for the thinner one with rounded geometry. Larger values of n were also apparent when the larger groove was used, but the evidence was very weak due to the large scatter and to lack of data. Moreover, some determinations of fracture toughness, K_{IC}, showed that the estimated values increase with groove width.

Atkinson [3] observed that a possible explanation of the larger scatter and fracture toughness could be the interaction between crack tip and guide groove walls. If the side groove is very narrow, the crack is constrained to follow a relatively straight path. A larger groove would allow the crack to wander, choosing the lowest energy path (eventually changing from transgranular to intergranular). For intermediate groove width the crack reaches the groove walls and it is sharply deflected towards the midplane. For larger width the crack is deviated more gently before reaching the groove walls. Furthermore, apparent crack velocity is decreased by the roughening of the crack path.

The conclusion seems to be that the groove should be omitted when possible. It is impractical, however, to eliminate side grooves in such heterogeneous materials as rocks.

5.2.6 Operational range of crack length

One of the main advantages of the DT specimen is that the relation between the *SIF* and the measured load appears to be independent of the crack length, and therefore constant along the test.

Actually this property was assessed to be valid only for sufficiently long cracks and ligament lengths $(L - a)$ [10], [36].

A finite-element study performed by Trantina [34] and some experimental DT tests performed by Shetty and Virkar [31] showed that Eq. (3.7) for the *SIF* overestimates K_I for short cracks, and underestimates it for long ones. The two studies determined an operational range for the crack length in which Eq. (3.7) is accurate within 5%. Grossly, the distance of the crack tip from both ends of the specimen should be larger than the specimen width W (for the details see section §7.4).

These misestimates derive from a deviation from linearity of the compliance when the crack is near the ends of the specimen. For very short cracks the deformation of the plate beyond the crack is no more little compared to the torsion of the two beams. For long cracks the plate beyond the crack becomes rapidly shorter, thus increasing the effect of its compliance.

5.2.7 Length to width ratio

The considerations in the previous section suggest that long specimens should be used with a length to width ratio at least larger than 2.

Furthermore, estimates of the stress corrosion index reported by Atkinson [3] for Westerly granite and Ralston basalt using specimens with $L/W \sim 2 - 2.5$ were on average 50% lower that the ones obtained by Swanson [32] on samples cut from the same blocks with $L/W \sim 6$.

On the other hand, the measures of Pabst and Weick [25] on Al_2O_3 material showed the opposite trend, but these measure were obtained using the constant load method rather than by load relaxation, so that the final effect on n could be different.

Chapter 6

Finite-element study of the Double Torsion specimen

6.1 The finite-element model

As we have observed, a substantial part of the scatter among different measurements is due to Evans' model not describing the effective deformation of a realistic DT specimen with sufficient accuracy.

For this reason, we decided to perform an accurate, three-dimensional finite-element analysis of a realistic specimen: that is, one with finite thickness, a groove, and an initial notch. The aim of the study was to estimate the influence on the strain energy release rate, G, of the specimen width and length, the fracture length, the presence and shape of the side groove, the presence of the initial notch, and the curved shape of the fracture front. Furthermore, no constraint on the state of strain of the crack tip should be assumed.

This type of approach was explored earlier by Trantina [34]. His results were interesting but not very useful in practice, because his study of 176 linear elements produced just five values of G, for a specific specimen with no side groove and no initial notch. Furthermore, his use of linear elements prevented him from obtaining a crack front with a realistic inclination.

6.1.1 Choice of the Physical quantity G

Evans' equation (3.7) is based on the computation of the strain energy release rate ($SERR$) by derivation of the compliance of the DT specimen. Then, he uses the plane-stress relationship $K_I = \sqrt{E \cdot G}$ to obtain the mode I stress intensity factor. Because the plane-stress assumption and the exact fracture

modality are, so far, not well understood in the *DT* loading configuration, direct measurement of the *SERR* in the finite-element simulation seems best for studying Evans' equation. The idea is to measure the difference, δU, in total strain energy for two meshes with a little difference, δa, in crack length and to normalize δU to the difference in the crack area. Thus,

$$G = -\frac{1}{d_n}\left(\frac{\delta U}{\delta a}\right)_y \tag{6.1}$$

Consequently, the mesh does not have to be very fine, because an extremely accurate representation of the deformation field around the crack tip is necessary only if the crack-surface displacement approach is used.

6.1.2 Finite-element code and computing resources

The present meshes were designed using a graphic editor (*Mentat 3.2*, produced by MARC Corporate, Palo Alto, USA) and analyzed using a parallel code (*Marc K7.3*, also produced by MARC Corporate). The solution process was very laborious, but it was made feasible by access to the powerful resources of the CINECA computing center (Consorzio Interuniversitario Nord-Est Calcolo Automatico, Bologna, Italy) and, in particular, a supercomputer (Model *Origin*^{TM} *2000*, produced by SGI^{TM}, USA) with 16 parallel CPUs (MIPS R10K 195 MHz), 8 gigabyte RAM, and a peak performance of 6.24 gigaflops. The operating system used was SGI^{TM} *Cellular IRIX 6.5.3*. Because this supercomputer used $\sim$ 5 CPU minutes to solve a model, the present study analyzed 1800 models in 150 CPU hours, obtaining 600 values of G that explored combinations of several different parameters.

6.1.3 Mesh design

The finite-element model is designed to represent a *DT* specimen in the constant displacement configuration. Because the model is symmetrical, the mesh describes only one half of the specimen (see Fig. 6.1). The model is made of $\sim$ 500 brick elements disposed in five slices, one of which is partially removed to simulate the presence of the side groove. The elements at the beginning of the groove are moved back to simulate the initial notch. The refined subdivision of the elements in the first row allows the positioning of the loading points (four-point bending).

The most sophisticated part of the design is the region surrounding the crack. The most common solution for representing cracks is to design a spider-web mesh around the crack front, with quarter-point nodes on the

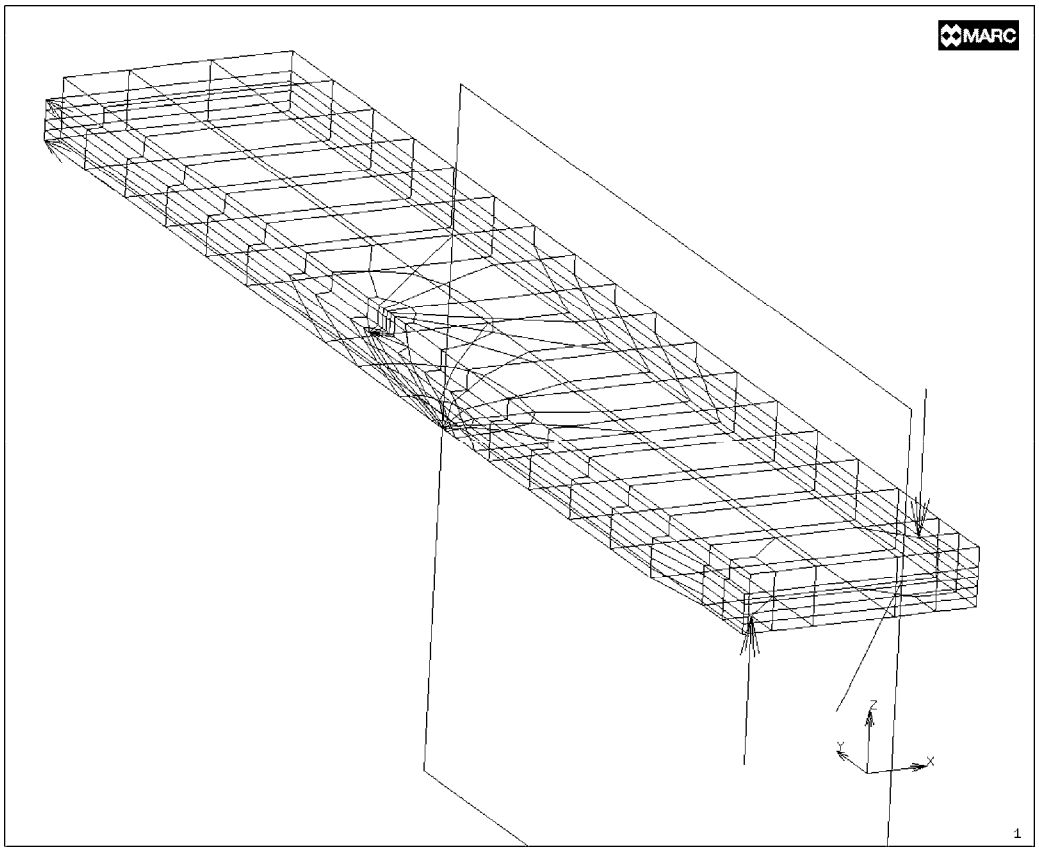

Figure 6.1: Finite-element mesh. The model represents one half of the *DT* specimen. The remaining part is replaced by symmetrical conditions and by a contact surface in the failed interface. The side groove and initial notch are reproduced. The crack front is designed by hand to reproduce the experimental shape.

first shell of elements. This solution allows for a better adaptation to the physical behavior of the strain field near the crack tip and was validated against the predictions of the analytical solution for the double cantilever beam [34].

Trantina [34] also used this spider-web mesh for the *DT* loading configuration, introducing a weak inclination of the fracture front. Because the strain field near the curved crack tip of the *DT* specimen was not known in detail, Trantina removed the inner shell of elements near the crack tip. In contrast, the present study involved first testing the elements with quarter-point nodes and then the normal elements; an attempt also was made to remove the inner shell. Because all of the variations in G generally were $< 1\%$ (with better consistency between quarter-point and normal elements), the simpler normal elements were used here. The radius of the inner shell of nodes is $R = 1.6$ mm ($R/d \approx 0.23$).

The geometry of the inclined spider web was matched carefully with the presence of the groove, and the internal position of each node was optimized, with the aim of reaching the maximum curved-front inclination allowed by the deformation limits of the elements (the graphic mesh editor Mentat has an internal element-check function that highlights elements whose distortion is above a threshold value).

For the low strain used in the present model, and assuming the use of second order elements, the code indicated a threshold value of 0.95. In regard to the distortion, this value indicated that the internal angles of each element could not decrease to <10°. In regard to the aspect ratio (the ratio between the surface and the volume of an element), the 0.95 threshold value meant that the ratio between the length of different sides of an element could not be >12.

These restrictions limited the extent of curvature of the crack profile. Experimental results have shown that the ratio of inclination, $c = \Delta a/d_n$, typically is ~5 [10]. In the present case, optimization allowed a maximum inclination at $c = 4$, a substantial improvement over the value $c = 1.7$ obtained by Trantina [34] with lower order elements. To simulate the curvature, a different inclination was used for each quarter of d_n. For the specimens with $c = 4$, the four inclinations were 30°, 20°, 10°, and 10°. A series of specimens with a straight front ($c = 0$) and a series with an intermediate inclination, $c = 2$ (angles of 49°, 34°, 19°, and 19°) also were designed to clarify the influence on G of global inclination. Figure 6.2 provides a close-up view of the crack tip for $c = 4$, along with a plot of the strain energy density field.

For the specimen represented by the basic mesh, shown in Fig. 6.1, L (length) = 17 cm, $W = 6$ cm, and $d = 7$ mm. The moment arm of the torsion was $w_m = 2$ cm. Longer specimens, with $L = 25$ cm, were generated by

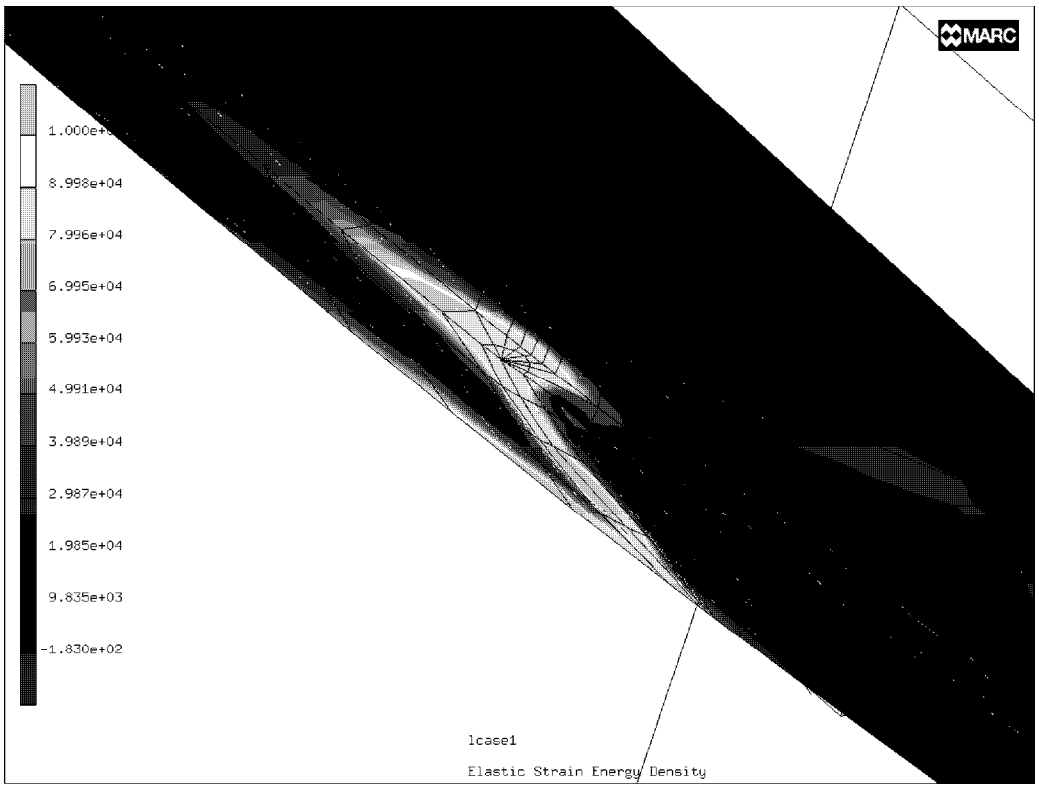

Figure 6.2: Plot of the strain energy density field near the fracture front. The energy is visibly concentrated along the curved front and inside the groove.

adding rows of elements. Wider specimens, with $W = 10$ cm, were generated by expanding the external row of elements, so that only the moment arm was changed, to $w_m = 3.5$ cm, leaving all the internal region containing the groove unaltered.

For each combination, five different crack lengths were obtained by moving the central part with the crack and resubdividing the elements of the remaining parts. The crack length values, a, were measured from the position of the loading points (in the present case, 0.5 cm from the beginning of the specimen) to the end of the crack on the lower opening side. For the shorter specimens, the crack length values were $a = 4.5$, 6.5, 8.5, 10.5, and 12.5 cm; for the longer specimens, the values were $a = 5.5$, 8.5, 12.5, 16.5, and 20.5 cm.

The width of the groove, w_g, was changed by incrementally decreasing the width of the corresponding row of elements from 4 mm to 2 mm. The change in depth of the groove, $g_d = 1 - d_n$, from one-third to one-half of the specimen thickness ($d/3$ to $d/2$), needed more attention: The whole slice under the groove was contracted in the z direction, but the central block surrounding the crack front also had to be contracted by the same amount along the direction of the groove, in order to preserve the same aspect ratio for the crack front profile relative to d_n. Specimens without grooves were produced by eliminating the first slice, expanding the remaining part in the z direction, and again expanding the central block along the direction of the groove.

All of the present specimens also were doubled in number, to create a version with an initial notch 2 cm long and another without a notch. The parameter values can be summarized as follows.

- 5 crack lengths: $a = 4.5$, 6.5, 8.5, 10.5, and 12.5 cm for $L = 17$ cm
  $a = 5.5$, 8.5, 12.5, 16.5, and 20.5 cm for $L = 25$ cm
- 3 front inclinations: $c = \Delta a/d_n = 0$, 2, and 4
- 3 groove depths: $g_d = 1 - d_n = 0$, d/3, and d/2
- 3 groove widths: $g_w = 0$, 2, and 4 mm
- 2 specimen lengths: $L = 17$ and 25 cm
- 2 specimen widths: $W = 6$ and 10 cm
- 2 notch lengths: $nl = 0$ and 2 cm

Combining all of these different parameters by Cartesian product resulted in 600 different models. For the computation of G, three meshes were produced for each model, moving forward the region around the crack front in two steps of 0.2 mm each. The two strain energy increases were verified to be consistent, and the strain energy release rate on the global increment was calculated.

The total number of meshes analyzed was 1800. To accelerate the design process, only 60 basic meshes were worked out individually with the graphic editor. All the other meshes were generated automatically by moving some sets of nodes with external C programs and Unix shell scripts expressly written for that purpose.

6.1.4 Boundary conditions

The load was applied using a four-point-bending scheme, by imposing a fixed vertical displacement onto the loading points, as shown in Fig. 6.1. The inner loading point on the bottom face was moved up of 0.15 mm, and the outer loading point on the top face was moved down of the same amount, so that the global displacement, y, was 0.3 mm. Because the deformation is not symmetrical with respect to the z direction, all other points had to be free to move vertically for the whole specimen to find its equilibrium position. To prevent other global translations or rotations of the model, two points at the end of the specimen were fixed in x and y direction (see Fig. 6.1).

The symmetrical boundary conditions at the interface between the two halves of the specimen were implemented in two steps:

(1) The nodes on the intact portion of the interface were bounded to move on a vertical plane.

(2) The nodes of the cracked portion were free to move away from the vertical plane, but they were bounded by a rigid contact surface that simulated the compressive effect against the other half of the specimen (see Fig. 6.1).

The contact surface started before the first node on the top side of the cracked surface. In the specimens with curved crack front, this positioning left out some nodes along the crack surface, but this omission is not cause of concern, because loading clearly would move the nodes away from the contact surface.

6.1.5 Element properties

For the present model, 20-node elements belonging to the *serendipity* family were used. These second order elements, characterized by the presence

of additional nodes in the middle of each edge, provided a good balance between rapidity of the convergence and computational cost. Full integration, based on five points, made the solution more accurate. The analysis was based on linear elasticity, with the physical properties of the material given by the values of Young's modulus, $E = 10^4 MPa$; Poisson's ratio, $\nu = 0.2$; and density, $\rho = 2.2$ Kg/dm^3.

6.2 Testing stability

For better control of the solution process, the load application was divided into 10 steps, a method that assured optimal linearity with load ($C = y/P$ was constant within 10^{-5}, as shown in Fig. 6.3). The convergence control was based on the displacement check. The program calculated the convergence ratio using the equation

$$CR = \frac{max(\delta u_i)}{max(du_j)} \tag{6.2}$$

where CR is the convergence ratio, δu_i the node-displacement increments in the last iteration, and du_j the final displacements. The present values of CR were always between $2 \cdot 10^{-12}$ and $4 \cdot 10^{-8}$, indicating excellent convergence, because the threshold proposed by the code supporters is 0.05. In this type of analysis, the displacement check is more significant than the residual force check, which is based on the ratio between the maximum residual force and the maximum reaction force. Because the load is applied only on two nodes, the maximum reaction force is always very high, resulting in very low convergence ratios.

Another important test index is the singularity ratio, SR, which is related to the conditioning number, C, of the system of linear equations to be solved with the Crout elimination process. The conditioning number is defined as the ratio between the highest and the lowest eigenvalues of the system. The SR is an upper bound for the inverse of the matrix conditioning number. Thus,

$$\frac{1}{SR} \leq C \tag{6.3}$$

The number of digits lost in the elimination process is $n_{lost} = -log_{10} SR$. The singularity ratios obtained in the present solution were always between $8 \cdot 10^{-7}$ and $1.8 \cdot 10^{-2}$; this result indicates a maximum loss of $\sim$6 digits. Because the code works in double precision (that is, with an internal accuracy of 10^{-12}), the first 6 digit are not affected by numerical approximations. The

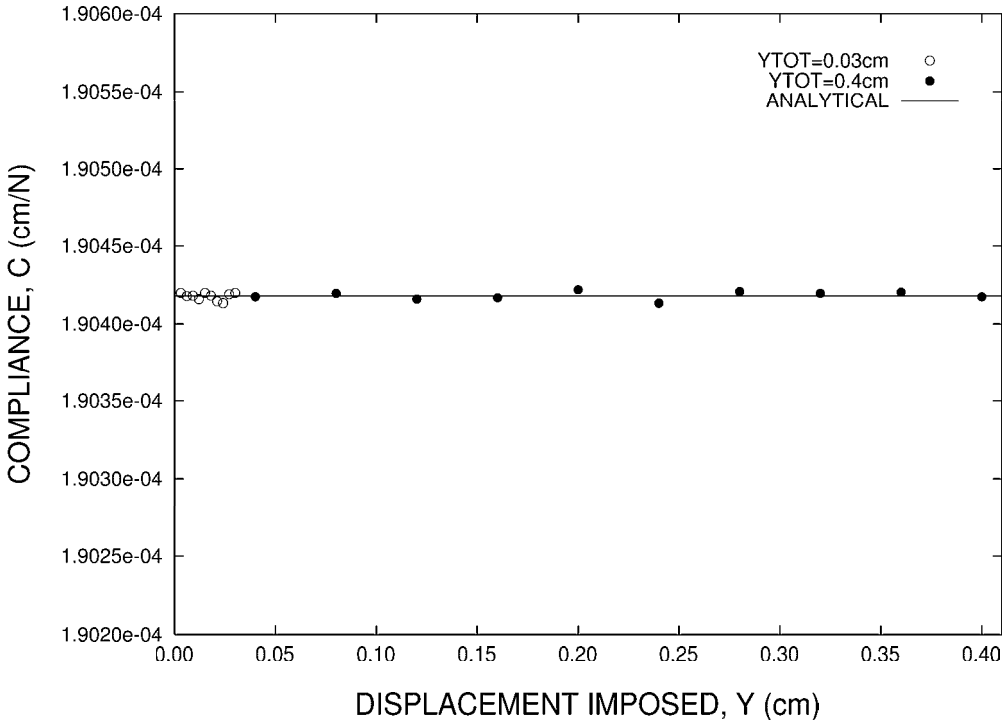

Figure 6.3: Test of the linearity in the loading configuration. The 10 open circles on the left represent the real load steps in the simulation (total displacement $y_{TOT} = 0.03$ cm). The 10 solid circles represent a test made with a higher total displacement $y_{TOT} = 0.4$ cm. The values of $C = y/P$ are constant within 10^{-5} in a region one order of magnitude larger than the one used.

numerical precision of the strain energy, U, then is $< 10^{-6}$, but the strain energy release rate is obtained from differences between two values of U with different crack length. The crack length increment chosen for the present study assured that such differences were never $< 0.1\%$ of the strain energy values. Thus, the numerical precision of the differences was always $< 10^{-3}$, a good result because the global accuracy of the present results was $\sim 1\%$.

The *full Newton-Raphson* iterative procedure was used to solve the meshes. To test the reliability of the procedure for the present case, some solutions were derived by using a *large-displacement procedure*, as well as an *updated Lagrange procedure*. The obtained results were consistent within 1%. The values of the total strain energy were obtained by integrating the strain energy density over the whole mesh. The high degree of linearity observed suggested the recalculation of the total strain energy also by the relation $U = yP/2$, where P is the reaction force at the loading points. The two

values were consistent within 10^{-5}, a proof of physical reliability. The consistency of the local trend of the strain energy caused by small displacements of the nodes during the calculation of G and the general trend of the strain energy among the five different crack lengths, also was checked.

To test the stability of the model, many different meshes, corresponding to the same geometric model, were designed. The number and position of the rows and the slices were changed, as well as the extension of the set of nodes that was moved along with the crack front. The variations obtained were always $< 1\%$, giving the present results a precision of 1%.

6.3 Results

The present results, consisting of 600 G values for all combinations of the different parameters, are reported in Tables A.1 to A.4 in the appendix as corrective factors, ψ, with respect to Evans' equation. Thus,

$$G = \psi \frac{w_m^2 P^2}{2\eta W d^3 d_n \mu} \tag{6.4}$$

More precisely, the finite-element value of G, G_{FE}, was evaluated using Eq. (6.1), where U is twice the total strain energy obtained by the finite-element analysis of the halved specimen. The load, P, was evaluated using the well verified equation $U = yP/2$, where y is the value of the constant displacement. Finally, the values for G_{FE} were divided by the analytical value, G_{AN}, obtained from Eq. (3.4) for the same load, P. The values of η for $W = 6$ cm and 10 cm were 0.285 and 0.304 respectively (see § 5.2.1).

Some of the present results are plotted on Figs. 6.4-6.4, to show the influence of each parameter. Clearly, the correction value is very important Variations from 10% to 50% are apparent for the five different crack lengths, with a clear increasing trend, in agreement with other experimental observations [26],[31] (see also § 5.2.6).

The use of three different front inclinations ($c = \Delta a/d_n = 0$, 2, and 4) produced very consistent results in the center of the specimen (Fig. 6.4). However, away from the center, the *SERR* varied by $\sim 8\%$ near the borders, and G increased with the inclination. The value of $c = 5$, observed in earlier experiments [10] was not obtained here, because the distortion of the elements around the crack tip was too high, but such a value could be reasonably expected to produce a slightly higher value of ψ.

Changes in the groove depth produced a general shift in the coefficients, accentuated for long cracks (Fig. 6.5). The *SERR* increased by $\sim 5\%$ when the groove depth increased from zero to one half of the specimen thickness.

This major effect clearly resulted from the weakening of the specimen. A similar effect influenced the dependence of G on groove width (G increased by $\sim 4\%$ when the groove width increased from 0 to 4 mm, as shown in Fig. 6.6).

The dependence if G on specimen dimensions was both important and complex. For all the specimen widths considered, short crack lengths exhibited consistent results, but the shorter specimen had an earlier deviation of ψ for large values of a (Figs. 6.7 and 6.8). This deviation shows that the increase in ψ for long cracks is some sort of an end effect. Furthermore, a comparison of Figs. 6.7 and 6.8 shows a higher deviation for the larger specimen. Both these results are in agreement with experimental observations [26],[31] and also with Fuller's [12] conclusion that such effects should be evaluated in terms of distance of the fracture tip from the ends of the specimen (expressed in units of widths) rather than in terms of the ratio between crack and specimen length.

The difference caused in the *SERR* by the presence of the initial notch was generally very weak, except for short crack length, in which it produced variations of $\sim 5\%$ (Fig. 6.9).

As a conclusion, the present finite-element analysis showed that the classical equation for describing DT fracture experiments is generally inadequate. The presence and shape of the side groove and of the initial notch, along with the crack front shape and the end effects, play a major role in affecting the strain energy release rate. The effect on G of all these parameters was examined exhaustively in the present study in terms of corrective coefficients of the classical equation. The importance of the corrections proved to be considerable (up to 40%) and likely a major cause of the large scatter between the $G - v$ curves measured in different laboratories.

In next section we will show how these coefficients can be actively used to correct the analysis if the whole method is adequately modified.

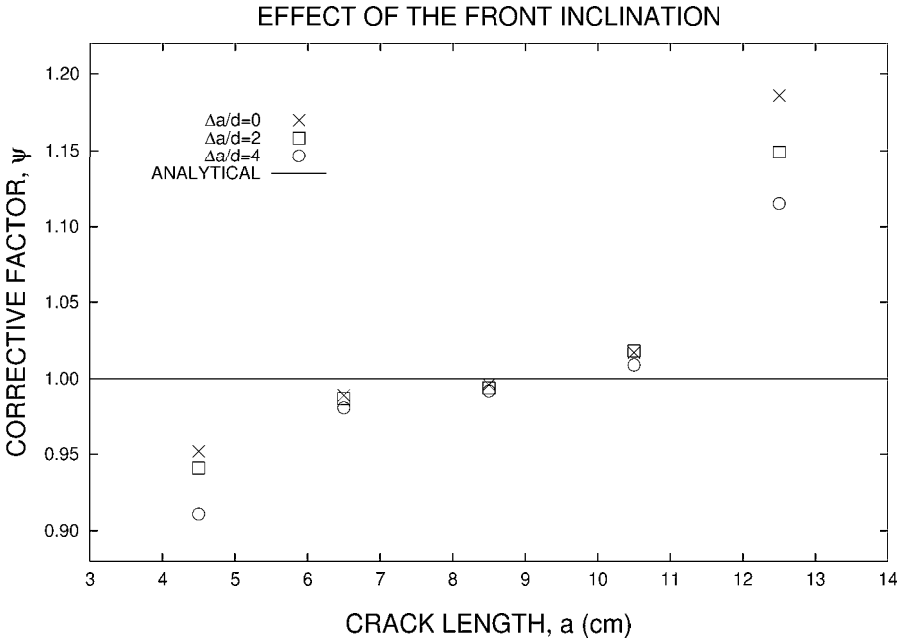

Figure 6.4: The corrective factors, ψ, as a function of front inclination, c, for five different crack lengths.

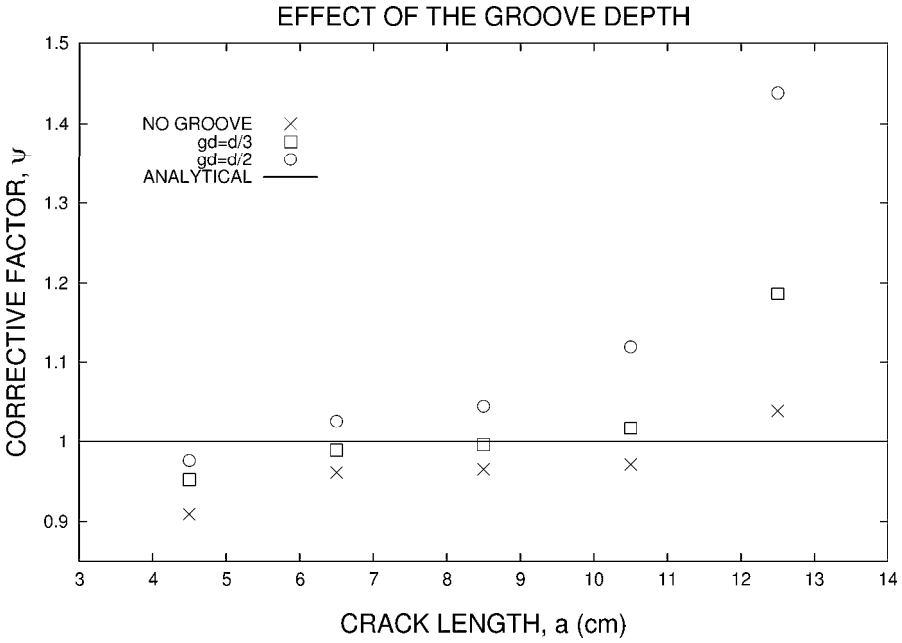

Figure 6.5: The corrective factors, ψ, as a function of groove depth, $g_d = (1 - d_n)$, for five different crack lengths.

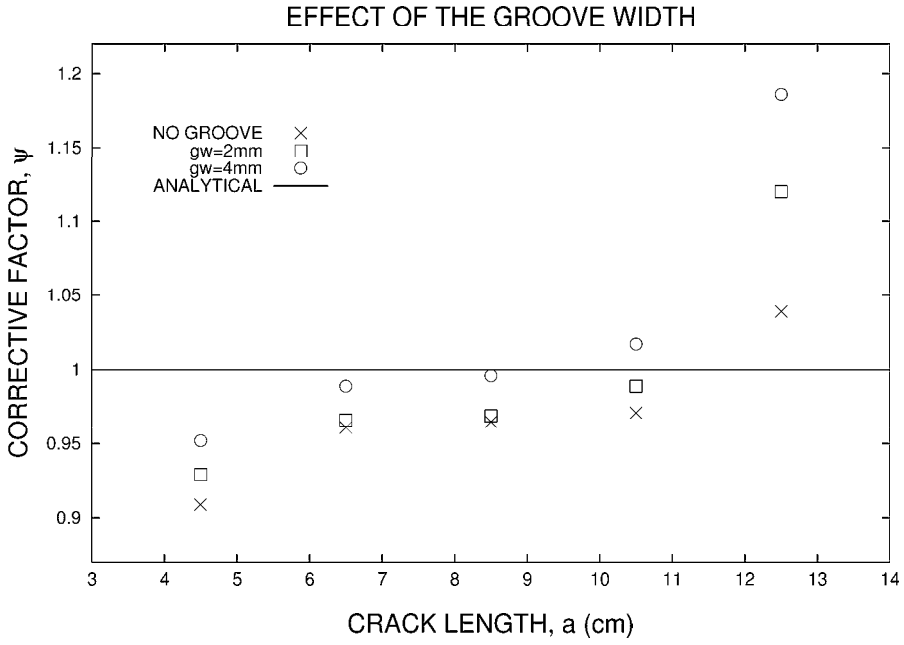

Figure 6.6: The corrective factors, ψ, as a function of groove width, g_w, for five different crack lengths.

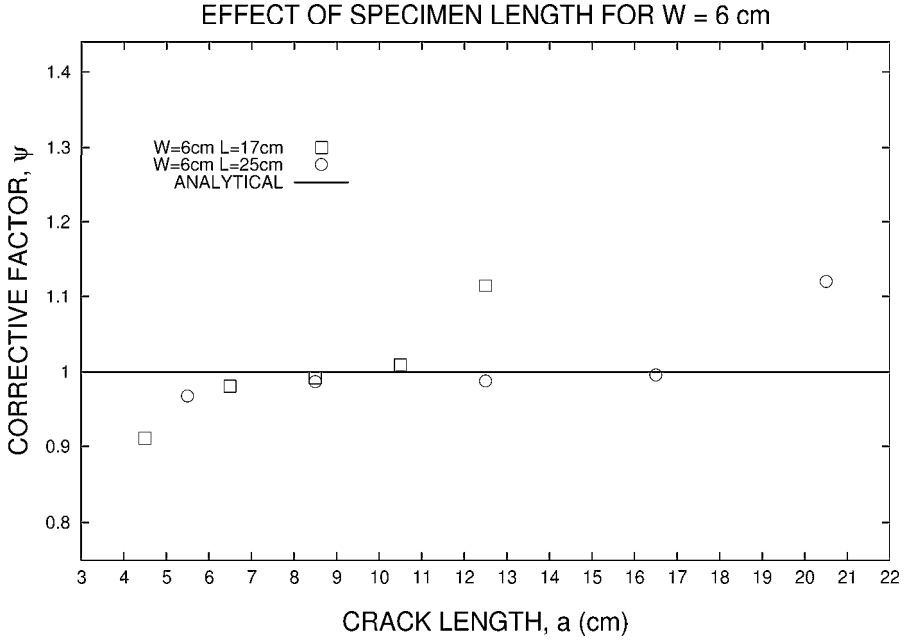

Figure 6.7: The corrective factors, ψ, as a function of specimen length, L, for $W = 6$ cm, and for five different crack lengths.

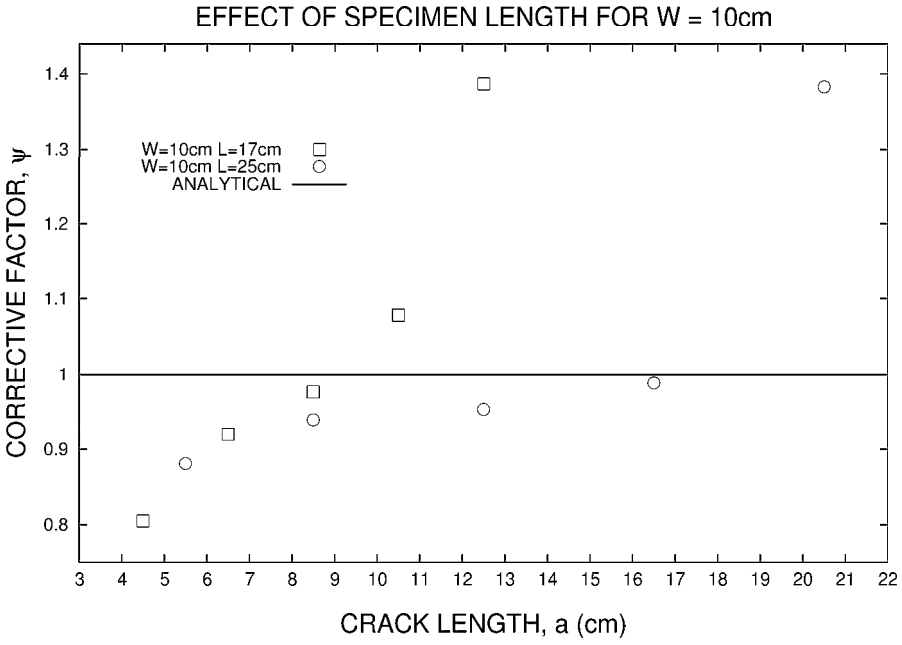

Figure 6.8: The corrective factors, ψ, as a function of specimen length, L, for $W = 10$ cm, and for five different crack lengths.

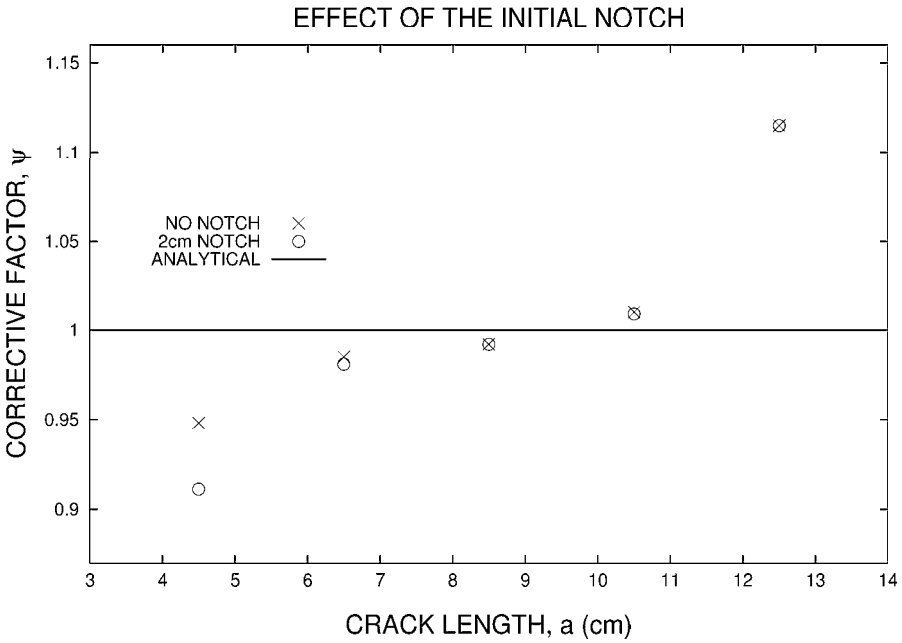

Figure 6.9: The corrective factors, ψ, as a function of notch length, nl, for five different crack lengths.

Chapter 7

Improved methodology for the load relaxation test

The aim of the present chapter is to define a new methodology for the analysis of the *DT* load relaxation tests, based on the use of the corrective coefficients obtained by the finite-element analysis and to describe its numerical implementation.

We already observed that the assumptions for the calculation of the *SIF* from G are not well understood (see § 6.1.1). However, because the stress-corrosion index n is defined as the slope of the logarithmic $K_I - v$ curve, we will use here the *SIF* to make the final comparison with preexisting data easier.

For a given specimen geometry, the corrective coefficients are dependent on the crack length, and therefore they are not constant during the relaxation test. As a consequence, the estimation of the *SIF* must be corrected during the test and, since the inversion of the crack velocity v is affected in a non-linear way, the $K_I - v$ curve and the stress-corrosion index result to be significantly altered.

7.1 Corrective factors ξ and ψ

Evans' model leads to a linear dependence of the compliance on the crack length a

$$C = \frac{y}{P} = \frac{w_m^2 a}{\eta W d^3 \mu} = Ba \tag{7.1}$$

where y is the constant displacement imposed at the loading points. Experimental compliance-calibrations [10] lead to a more general affine relation

$C = Ba + D$. Since the strain energy release rate

$$G = -\left(\frac{dU}{dA}\right)_y = \frac{P^2}{2d_n}\frac{dC}{da} \tag{7.2}$$

is related to the first derivative of the compliance, it appears to be independent of the crack length.

Our finite-element analysis showed that the dependence of C on the crack length contains some weak nonlinear terms, hardly appreciable through experimental compliance-calibrations, which nevertheless produce significant variations in the first derivative, making the strain energy release rate dependent on the crack length.

In order to account for such non-linear terms, a corrective factor ξ dependent on the crack length a has been introduced in Evans' equation for the compliance

$$C(a) = \frac{y}{P} = \xi(a)Ba = \xi(a)C^E(a) \tag{7.3}$$

where the superscript E stands for "Evans' model" and B is the proportionality constant of Eq. (7.1). Taking the first derivative of Eq. (7.3), another corrective coefficient ψ is obtained that has to be applied to Evans' equation for the constant-displacement strain energy release rate (after Eq. (7.2))

$$G_y(a,P) = \left(\xi(a) + a\frac{d\xi(a)}{da}\right) G_y^E(P) = \psi(a)G_y^E(P) \tag{7.4}$$

This coefficient ψ is the one discussed in the previous chapter. The coefficient ξ was not considered in a first time because it does not affect the strain energy release rate. However, since it will be shown to be relevant for the determination of the crack velocity, the values of ξ for all the combinations of geometrical parameters are reported in Tables A.5 to A.8.

The values of ξ and ψ as a function of crack length for specimens with length $L = 17$ cm and width $W = 6$ cm are plotted in Figs. 7.1 and 7.2 as an example. The shape of the function $\psi(a)$ is characterized by a positive trend with a flatter region in the center of the specimen, and strong deviations moving towards the ends. The scatter introduced by the dependence on the geometric parameters is considerable.

The overall behavior of the corrective functions can be understood as follows. Using the two independent torsion bars model, the compliance falls linearly to zero together with the length a of the bars. In real specimens with short cracks, the deformation also affects the region beyond the crack, so that the compliance is larger and its slope is lower. As a consequence,

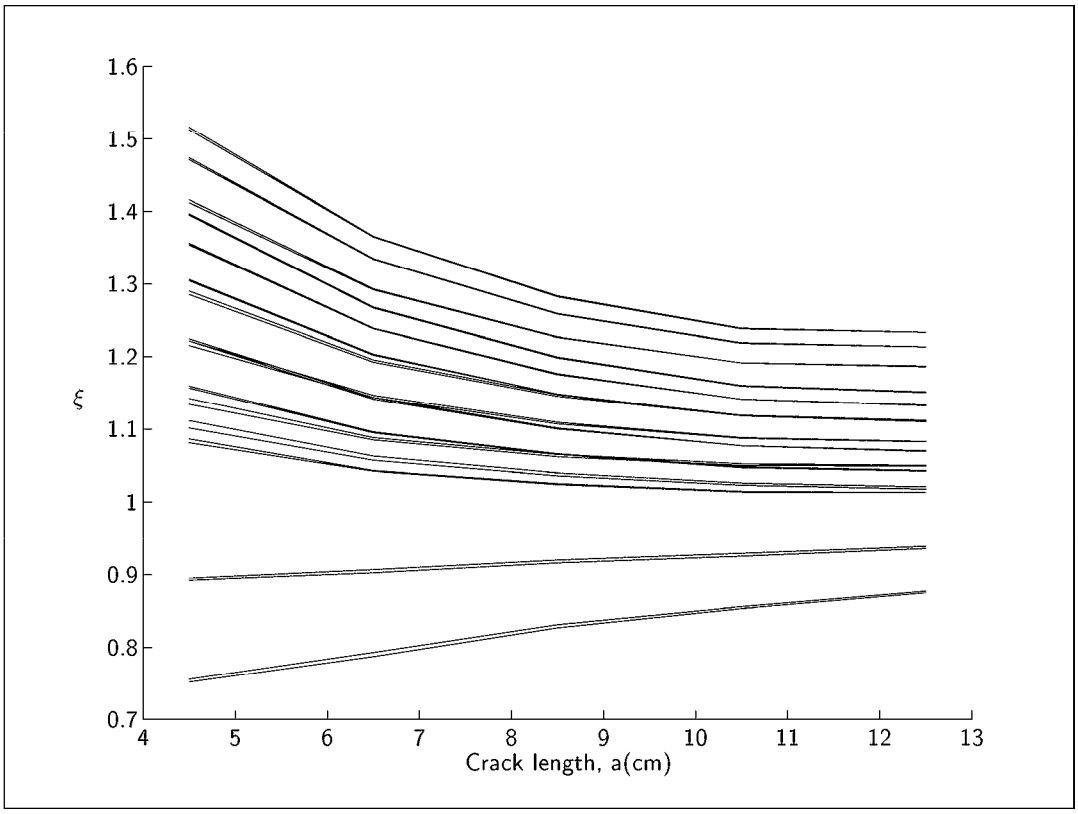

Figure 7.1: The corrective coefficients ξ for specimens with length $L = 17$ cm and width $W = 6$ cm. The different curves represent all combinations of the other geometric parameters.

when the crack length approaches zero, ξ increases and diverges to infinity and ψ decreases towards zero. When the crack approaches the end of the specimen, the unfractured portion becomes very weak, so that the compliance increases faster than predicted by Evans' equation, and diverges when the crack reaches the end (i.e. when the specimen fails). As a consequence, both ξ and ψ diverge to infinity for $a \to L$.

7.2 New equations for K_I and v

We will now discuss how the introduction of crack-length dependent corrective factors affects the estimates of K_I and v. As far as the mode-I *SIF* is concerned, the square root of the corrective coefficients ψ should be used (see Eq. (3.5)):

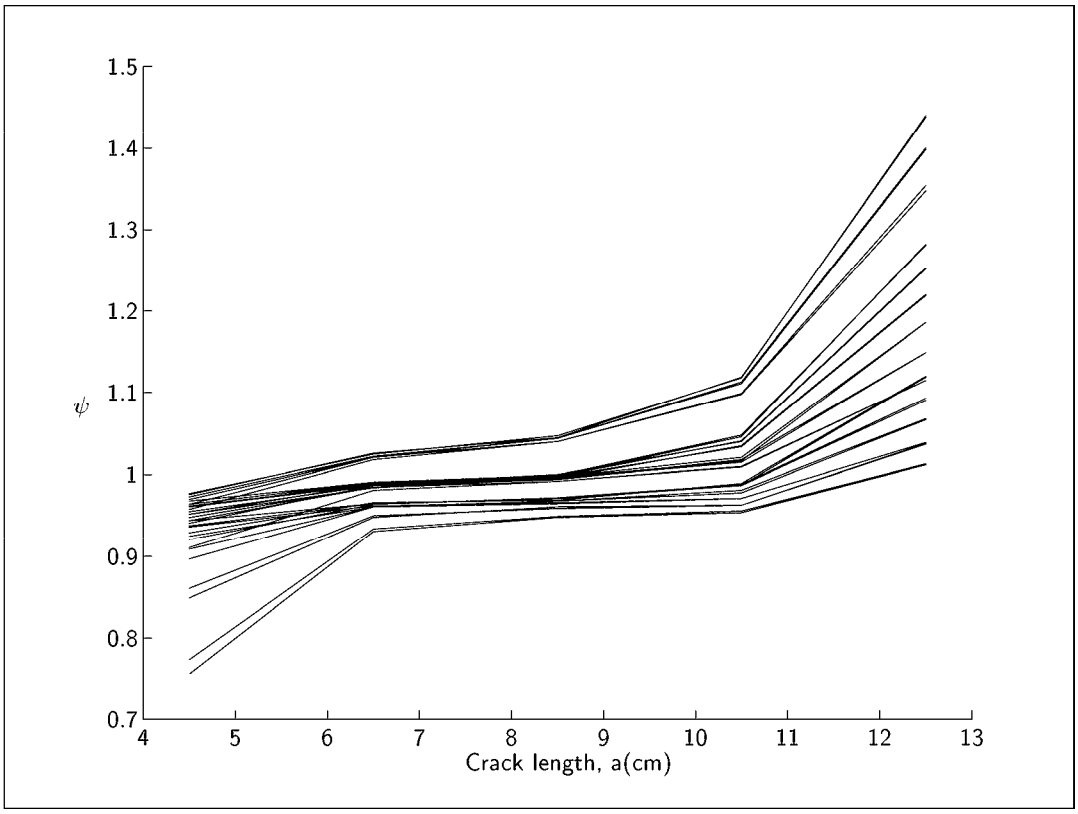

Figure 7.2: Same as in Fig. 7.1 for the corrective coefficients ψ.

$$K_I(a,P) = \sqrt{\psi(a)} K_I^E(P) \tag{7.5}$$

The calculation of the crack velocity is based on the derivation of the crack length $a(t)$, which is inverted from the load relaxation curve $P(t)$, through the constant displacement condition. Differentiation of Eq. (7.3) for constant displacement leads to

$$\left(\frac{da}{dt}\right)_y = -\frac{\xi(a)}{\psi(a)} \frac{a}{P} \frac{dP}{dt} \tag{7.6}$$

where $P(t)$ is the measured relaxation load, and $a(t)$ has to be inverted from $P(t)$ using the relation

$$y = C(a(t)) \cdot P(t) = C(a_{i,f}) \cdot P_{i,f} \tag{7.7}$$

where y is the constant displacement, and the subfixes i or f again denote

a reference measurement taken at the beginning or at the end of the test. Thus,

$$a(t) = C^{-1}\left(\frac{C(a_{i,f}) \cdot P_{i,f}}{P(t)}\right) \tag{7.8}$$

Substituting Eq. (7.8) into Eq. (7.6) and multiplying by the appropriate factor ϕ we obtain:

$$v = \phi\left(\frac{da}{dt}\right)_y = -\phi\frac{\xi(a_{i,f})}{\psi\left(C^{-1}\left(\frac{C(a_{i,f})\cdot P_{i,f}}{P}\right)\right)}\frac{a_{i,f}P_{i,f}}{P^2}\frac{dP}{dt} \tag{7.9}$$

Equation (7.8) also has to be substituted into Eq. (7.5) to calculate the *SIF* as a function of time, and thus produce the subcritical crack-growth curve $K_I - v$.

The above corrections affect both K_I and v in a non-linear way which changes the overall shape of the logarithmic $K_I - v$ curve, both in its location and slope. The corrections reduce K_I in the first part of the test, when it is larger, and increase it when it is lower, thus resulting in a rise in the slope, i.e. the stress-corrosion index n, in agreement with [31]. Note that the correction on the crack velocity v also affects the slope through the ψ coefficient in Eq. (7.9), which increases with a during the test. As a result, initial large velocities are increased and final low velocities are decreased, so that the slope n is further increased. The practical importance of the corrections to be applied to the stress-corrosion index n will be discussed in the following.

7.3 Numerical implementation

For each set of geometrical parameters, the finite-element analysis produced a set of five corrective coefficients ξ for the compliance and five coefficients ψ for its derivative, relative to different crack lengths.

The first operation is to determine a set of coefficients for the geometry of the specific specimen used in the test. In other words, the specimen geometry has to be interpolated from the set of tabulated geometries. Linear interpolation is generally adequate, except for the effect of specimen length which requires a scaling of the crack length.

The scaling of the crack lengths corresponding to the five corrective coefficients can only be effected for specimens with the same ratio d:W:L explored here. Extrapolations far from such ratios would require further numerical analysis. Note that the scaling also affects the length of the notch and the

position of the loading points, which has to be taken as a new reference for the measurement of the crack length.

Provided that the notch extends towards the center of the specimen past the loading points, the external part of the specimen does not affect the strain energy. As a consequence, the part of the notch that should be compared among different specimens is the one exceeding the position of the loading points. For example, if the notch is 2 cm long and the loading points are 0.5 cm from the end of the specimen, the effective length is 1.5 cm.

In Tables A.1-A.8 some coefficients are missing. These correspond to the shortest crack length of notched specimens without groove, for which the meshes could not be drown since the large horizontal extension of the curved crack front would make it intrude in the initial notch. But these missing coefficients are necessary for the interpolation process, and their values were estimated by combining the coefficients relative to the corresponding unnotched specimens together with the weak effect of the presence of the notch observed on specimens with deeper grooves. The results are reported in Table A.9.

The maximum crack front inclination in our numerical analysis was $c = \Delta a/d_n = 4$ due to the limitations in the skewness of the elements, necessary to perform an accurate numerical analysis. Even though the typical front inclination is $c = 5$ [10], the use of the finite-element analysis with $c = 4$ is recommended in order to guarantee reliable solutions.

Through interpolation among the lines of coefficients reported in the tables, we have now determined the set of five ψ and ξ values for the appropriate specimen geometry along with the five corresponding values of the crack length. Since the crack propagates during the experiment, both coefficients should be fitted with smooth functions of the crack length.

An appropriate choice for smoothing the corrective factors $\psi(a)$ appears to be a least-squares third-degree polynomial fit. The corrective coefficients ξ are best approximated by fitting the normalized compliance $\xi(a) \cdot a$ first. This can be done integrating the polynomial which fits ψ and choosing the constant to match the central coefficient. In this way, approximation inaccuracies below 1% on both coefficients can be obtained. Nevertheless, such a choice may sometimes produce appreciable errors on the values of ξ, especially at small or large crack lengths. If this is the case, a second-order polynomial fit for the normalized compliance will produce more accurate results. Any extrapolation out of the range explored by the present analysis is not recommended.

The interpolating function for the compliance has to be used together with the measurement of the initial or final reference point $a_{i,f}$, $P_{i,f}$, to invert the evolution of the crack length $a(t)$ from the relaxation data $P(t)$,

using Eq. (7.7).

Finally, the corrected values of K_I and v during the relaxation test are calculated, and the complete $K_I - v$ curve is obtained. Then, the data related to region III should be isolated, and the stress-corrosion index n can be calculated by a least-squares linear fit.

7.4 Operational geometric constraints

The non constancy of the *SIF* along the specimen was already pointed out in the literature [31], [34], a problem which was practically tackled by assuming an operational range for the crack length in which the classical Evans' analysis could be used. The operational range was defined as the one in which the *SIF* remained constant within 5%.

According to the above constraint, the experimental study of Shetty and Virkar [31] determined as operational the following ranges of crack lengths

$$0.50W < a < L - 1.00W \quad for \quad d : W : L = 1 : 31.25 : 75$$

$$0.40W < a < L - 0.80W \quad for \quad d : W : L = 1 : 50 : 75$$

The finite-element study of Trantina [34] determined the range:

$$0.55W < a < L - 0.65W \quad for \quad d : W : L = 1 : 10 : 20$$

The present numerical study allows a detailed and comprehensive analysis of the dependence of the operational range on the geometrical properties of the specimen (see Tables 7.1 and 7.2). A general dependence on the d:W:L ratio may be observed. At the same time, the depth and width of the groove are also important, while the presence of the initial notch has lesser effects. Only the ranges relative to the skewest crack fronts ($c = 4$) have been reported because they are the only one close to the real shapes.

The range determined by Trantina was calculated for model specimens with a weak front inclination $c = 1.7$ and should be compared with the ranges $0.50W < a < L - 0.68W$ and $0.76W < a < L - 0.70W$ obtained in the present study respectively for $c = 0$ and $c = 2$ relative to specimens without notch and groove and with a d:W:L ratio of 1:8.6:24.3. The comparison can only be partial since the d:W:L ratios are not coincident and the position of the loading points was presumably taken at the end of the specimen in Trantina's simulation. A detailed comparison with the ranges determined by Shetty and Virkar [31] is also impossible since their specimens are thinner than the ones considered here.

L	W	d_n/d	g_w	nl	$\frac{a_{min}}{W}$	$\frac{L-a_{max}}{W}$
17	6	1	0	0	0.89	0.66
17	6	2/3	2	0	0.57	0.76
17	6	2/3	4	0	0.58	0.80
17	6	1/2	2	0	0.59	0.95
17	6	1/2	4	0	0.69	1.01
17	6	1	0	2	0.91	0.66
17	6	2/3	2	2	0.69	0.75
17	6	2/3	4	2	0.71	0.80
17	6	1/2	2	2	0.62	0.95
17	6	1/2	4	2	0.70	1.01
17	10	1	0	0	0.61	0.54
17	10	2/3	2	0	0.47	0.64
17	10	2/3	4	0	0.48	0.66
17	10	1/2	2	0	0.49	0.69
17	10	1/2	4	0	0.54	0.72
17	10	1	0	2	0.62	0.53
17	10	2/3	2	2	0.52	0.64
17	10	2/3	4	2	0.54	0.66
17	10	1/2	2	2	0.54	0.69
17	10	1/2	4	2	0.59	0.72

Table 7.1: The crack length operational range defined as the region in which the variations of the *SIF* with respect to the center of the specimen are within 5%. The symbols are the same as in Table A.5. The specimen thickness is d = 7 mm, and the crack front inclination is $c = 4$ for all specimens.

7.5 The "true" value of the stress-corrosion index

In order to investigate the effect of neglecting the use of the corrective coefficients, as it happened so far in all analyses, some relaxation experiments have been simulated numerically. A theoretical region III of a $K_I - v$ curve was assumed with the functional form [10]

$$v = A \cdot K_I^n \tag{7.10}$$

with the values of the parameters $n = 40$ and $A = 10^{-3} ms^{-1}$, chosen as in typical lava rocks (see Table 4.3).

Two specimens where simulated with geometries chosen in the explored

L	W	d_n/d	g_w	nl	$\frac{a_{min}}{W}$	$\frac{L-a_{max}}{W}$
25	6	1	0	0	0.77	0.59
25	6	2/3	2	0	0.33	0.77
25	6	2/3	4	0	0.39	0.90
25	6	1/2	2	0	0.45	1.12
25	6	1/2	4	0	0.52	1.23
25	6	1	0	2	0.77	0.58
25	6	2/3	2	2	0.39	0.78
25	6	2/3	4	2	0.45	0.88
25	6	1/2	2	2	0.48	1.11
25	6	1/2	4	2	0.53	1.23
25	10	1	0	0	0.60	0.63
25	10	2/3	2	0	0.44	0.76
25	10	2/3	4	0	0.45	0.79
25	10	1/2	2	0	0.43	0.86
25	10	1/2	4	0	0.44	0.91
25	10	1	0	2	0.64	0.63
25	10	2/3	2	2	0.48	0.76
25	10	2/3	4	2	0.49	0.78
25	10	1/2	2	2	0.47	0.85
25	10	1/2	4	2	0.48	0.90

Table 7.2: Continuation of Table 7.1.

set of parameters and the corresponding corrective curves were interpolated as described above. The first simulated specimen, 'Specimen 1', had geometrical parameters $L = 17$ cm, $W = 10$ cm, $d = 7$ mm, $d_n/d = 1/2$, $g_W = 2$ mm, $nl = 2$ cm, and c=4. The second simulated specimen, 'Specimen 2', had parameters $L = 25$ cm, $W = 10$ cm, $d = 7$ mm, $d_n/d = 1$, $g_W = 0$ mm, $nl = 2$ cm, and c=4.

The third-order polynomials fitting the coefficients ψ for the two specimens were respectively

$$\psi_1(a) = 4.504 \cdot 10^{-4}a^3 - 1.690 \cdot 10^{-2}a^2 + 2.094 \cdot 10^{-1}a + 3.990 \cdot 10^{-2} \quad (7.11)$$

and

$$\psi_2(a) = 3.219 \cdot 10^{-3}a^3 - 6.977 \cdot 10^{-2}a^2 + 5.274 \cdot 10^{-1}a - 3.988 \cdot 10^{-1} \quad (7.12)$$

The interpolating functions for the ξ coefficients were determined by interpolating the normalized compliance $\xi(a)\cdot a$ with a second-order polynomial fit, and then dividing it by a. Respectively

$$\xi_1(a) = 5.991 \cdot 10^{-3} a + 8.100 \cdot 10^{-1} - 1.168 \frac{1}{a} \tag{7.13}$$

and

$$\xi_2(a) = 3.106 \cdot 10^{-2} a + 5.480 \cdot 10^{-1} + 2.881 \frac{1}{a} \tag{7.14}$$

The corrective functions of the *SIF* for the two specimen geometries are plotted in Figs. 7.3 and 7.4. The operational ranges are indicated in these figures, together with the ranges explored by our finite-element study.

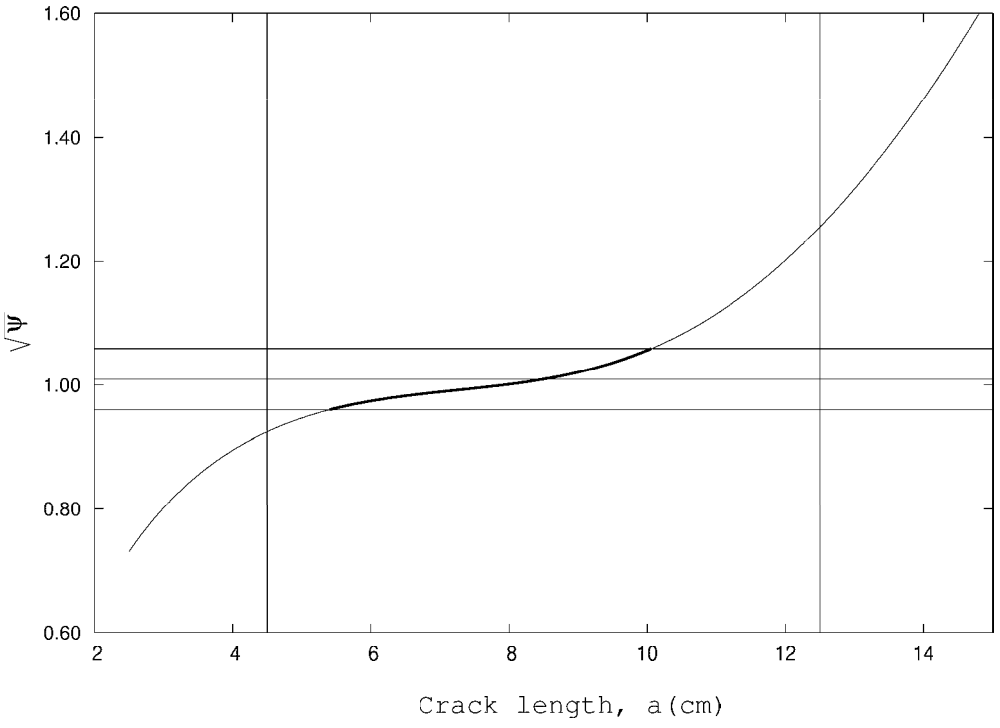

Figure 7.3: The corrective function for the *SIF* for the geometry called 'Specimen 1' The vertical lines delimit the range explored in the present analysis. The horizontal lines define the operational range in which K_I is constant within 5% (thick line).

Several relaxations of 100 seconds each were simulated, using an initial load $P = 100$ Kg and different values of the initial crack length.

The scheme of the simulation was as follows:

(a) use Eqs. (7.5) and (3.7) to derive the *SIF* K_I from the initial load P, with the corrective coefficient ψ calculated on the initial crack length;

(b) use the theoretical relation (7.10) to obtain the crack velocity v;

(c) increment of the crack length about $da = v \cdot dt$ where dt is the time step of the simulation;

(d) calculate the new load corresponding to the new crack length using Eq. (7.7);

(e) repeat from (a).

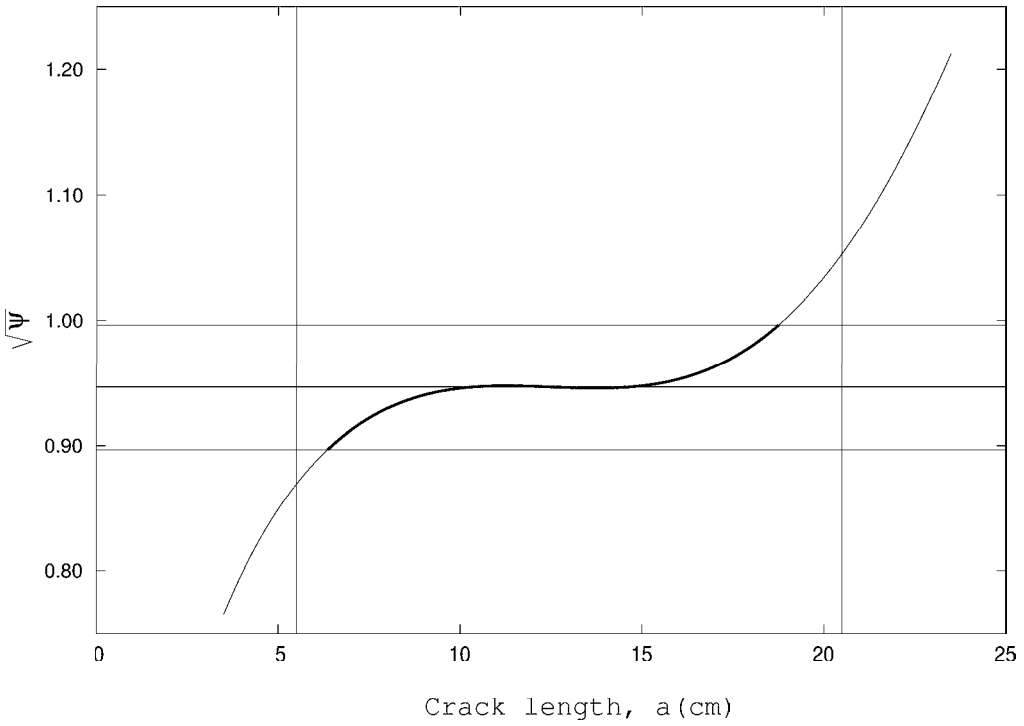

Figure 7.4: Same as in Fig. 7.3 for the geometry called 'Specimen 2'

The relaxation curves obtained were then analyzed with the classical Evans' method producing the $K_I - v$ curves reported in Figs. 7.5 and 7.6 together with the theoretical curve (thicker line). Substantial differences and a remarkable scatter are immediately apparent. Increasing the initial crack length, the location of the estimated curves moves progressively upwards in the bilogarithmic $K_I - v$ diagram. The shape of the curve gradually departs from linearity when the crack tip is near the borders of the explored range.

In fact, in these regions the corrective coefficient ψ is rapidly changing in a non-linear way as the crack length increases during the test. The slope of those curves is reduced proportionally to the local slope of the corrective curve $\psi(a)$. The values of the stress-corrosion index of such curves were calculated by a least-squares linear fit and the results are reported in Table 7.3. To test the stability of the results, the simulations were performed with two different time steps (0.5s and 0.1s), and consistent results were obtained.

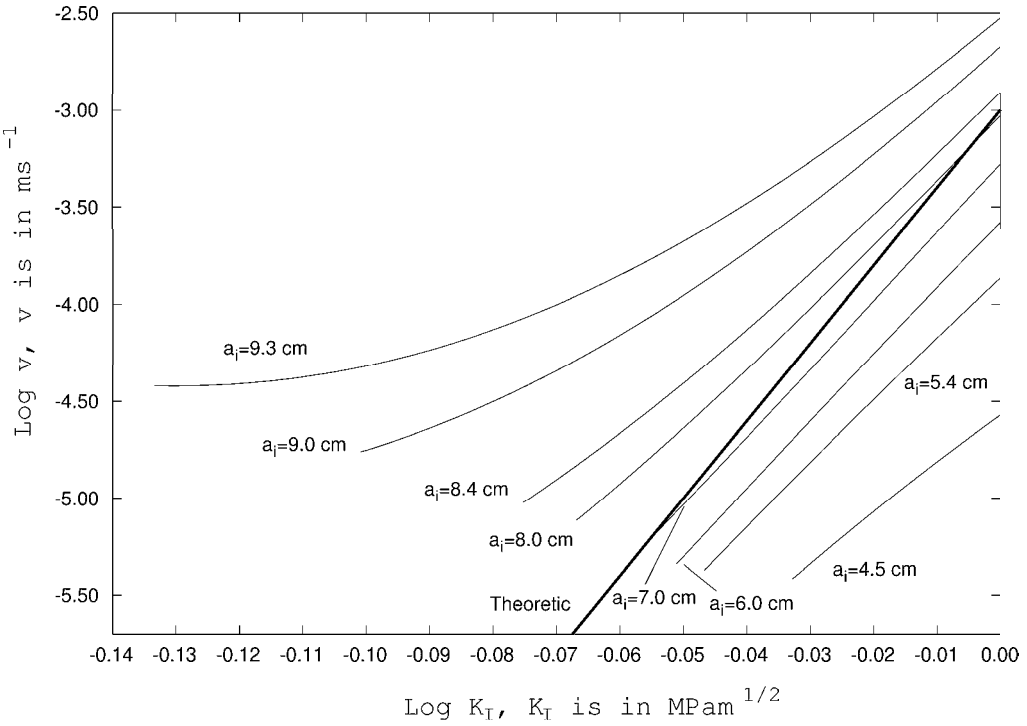

Figure 7.5: The $K_I - v$ curves obtained by applying Evans' analysis to some relaxation experiments simulated with the aid of the corrective curves for the Specimen 1. The initial load is the same for all experiments, the different values of the initial crack length are indicated for each curve.

The simulations in which the initial and final crack lengths were both within the conservative operational range (in which the *SIF* is constant within 5%) are indicated with a symbol 'v' in Table 7.3. The first important result is that Evans' analysis underestimates the stress-corrosion index up to 30% even operating in this range. As a consequence, this definition of the operational range is insufficient for accurate estimates of the stress-corrosion index with the classical Evans' approach.

An attempt to salvage the classical Evans' approach could still be made by defining a new operational range in which the underestimate on n itself

Specimen 1	$a_i(cm)$	$a_f(cm)$	n	$logA$	match
Real parameters			40.0	-3	
Operational range	5.4	10.1			
Explored range	4.5	12.5			
Estimated parameters	4.5	5.1	25.8	-4.5	x
	5.4	6.2	32.3	-3.8	v
	6.0	7.0	34.5	-3.6	v
	7.0	8.1	35.1	-3.3	v
	8.0	9.4	31.3	-3.1	v
	8.4	10.0	28.3	-3.0	v
	9.0	11.3	20.9	-2.8	x
	9.3	12.4	14.4	-2.8	x
Specimen 2	$a_i(cm)$	$a_f(cm)$	n	$logA$	match
Real parameters			40.0	-3	
Operational range	6.4	18.8			
Explored range	5.5	20.5			
Estimated parameters	5.5	5.6	33.2	-5.3	x
	6.0	6.2	33.8	-5.0	x
	6.4	6.6	34.3	-4.8	v
	7.0	7.3	35.1	-4.5	v
	8.0	8.5	36.5	-4.2	v
	9.0	9.6	37.9	-4.0	v
	10.0	10.7	39.0	-3.9	v
	11.0	11.7	39.9	-3.9	v
	12.0	12.7	40.3	-3.9	v
	13.0	13.8	40.1	-3.9	v
	14.0	14.8	39.1	-3.9	v
	15.0	15.9	37.1	-3.9	v
	16.0	17.1	33.8	-3.8	v
	17.1	18.6	28.5	-3.6	v
	18.1	20.4	21.2	-3.3	x

Table 7.3: The power law parameters obtained by linear fit of the $K_I - v$ curves in Figs. 7.5 and 7.5. The geometrical parameters of Specimen 1 were $L = 17$ cm, $W = 10$ cm, $d = 7$ mm, $d_n/d = 1/2$, $g_W = 2$ mm, $nl = 2$ cm, $c = 4$. Specimen 2 had $L = 25$ cm, $W = 10$ cm, $d = 7$ mm, $d_n/d = 1$, $g_W = 0$ mm, $nl = 2$ cm, $c = 4$. The initial and final crack lengths for each test were reported and a symbol 'v' was marked in last column if the whole relaxation took place inside the range in which K_I is constant within 5%.

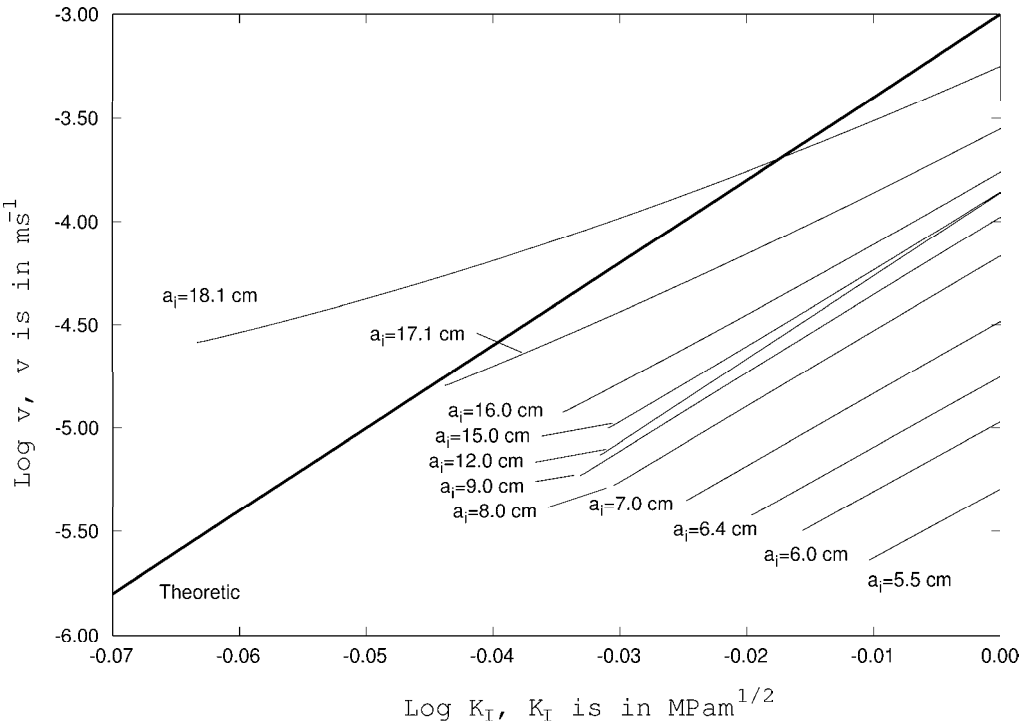

Figure 7.6: Same as in Fig. 7.5 for the Specimen 2

is limited to 5%. Unfortunately, for Specimen 1, the smaller error obtained for n is about 12%, making the definition of such a range impossible. As for Specimen 2, the errors on n could be limited to 5% only if the whole relaxation were performed in a very narrow operational range of crack lengths (from 9 cm to 15 cm on a 25 cm long specimen, see Table 7.3). This constraint is a very stiff one, since the attempts to produce an initial crack with a length in such a tight range would lead to discard most specimens. Moreover, the possibility of performing multiple relaxation tests on the same specimen would be considerably reduced.

On the contrary, by applying our corrective procedure there is no need to comply to such tight constraints, since the use of the corrective curves allows one to obtain accurate results working in a range that is much larger than the one required to obtain reliable estimates of n by using the classical Evans' method. The range left unexplored by our finite-element analysis is just five centimeters from each end of the specimen, which, for example, implies operational crack lengths covering a comfortable 15 cm range on 25 cm-long specimens. Table 7.3 shows that in this interval the classical Evans' analysis would produce underestimates up to 65%.

Chapter 8

Conclusions

8.1 What have we learnt?

While fracture is the physical process ruling many geophysical phenomena, it is so complex that developing theoretical models which can be effectively applied in practice has proved so far to be an impossible task. Furthermore, even the applicability of the models which have been developed has been hampered by the lack of a sufficiently accurate knowledge of fracture parameters.

We have focused our interest on this problem, attempting to improve the existing experimental techniques for the measurement of fracture parameters. We started from the most reliable experimental procedure, double torsion load relaxation method, and optimized several experimental aspects. These ranged from mere mechanical features like the stiffness of the loading machine, to the tight control of the environment, to data acquisition and inversion procedures.

This optimization has been apparently successful and allowed us to measure the subcritical fracture propagation index n with good coherence and repeatability (standard deviations of order 20%).

The finite-element analysis showed that the classical equation for describing DT fracture experiments is effectively inadequate. The presence and shape of the side groove and of the initial notch, along with the crack-front shape and the end effects, play a major role in affecting the specimen compliance and, therefore, the determination of all other quantities, such as the strain energy release rate, the stress intensity factor and the crack velocity.

The effect of all these parameters on the specimen compliance was identified exhaustively in terms of corrective coefficients for the classical equation. Although the deviations from linearity of the compliance as a function of

crack length are not so large, the consequences on the determination of all the other quantities proved to be substantial. The deviations of G and K from Evans' equations were up to 40% in the explored range of parameters. Following the approach of Trantina [34] and Shetty *et al.* [31], the operational range of the crack length in which the stress intensity factor is constant within 5% was determined as a function of all geometrical parameters, and this has shown that the definition of such operational range is not sufficient for the classical method to produce accurate results in the estimate of the stress-corrosion index.

We have shown first of all that the equation for the crack velocity should also be corrected. Second, since the corrective coefficients depend on crack length, both the corrections on K_I and v vary during the relaxation test. As a consequence, the $K_I - v$ curves result significantly altered. The most important result is that not only the location of the curves is changed, but their shape is also altered, resulting in a systematic increase in the slope. In other words, the classical Evans' method systematically underestimates the stress-corrosion index, which is considered as the most important parameter of subcritical crack-growth.

According to two numerical experiments of load relaxation tests that we performed, the neglection of the corrective coefficients leads to underestimating the stress-corrosion index up to 30% even if the relaxation takes place in the classical "optimal" operational range of crack lengths, where the variations of K_I do not exceed 5%. On the contrary, the use of the corrective coefficients allows one to obtain accurate estimates by using a wide range of specimen geometries and operational crack lengths.

8.2 An already published example

In section § 5.2.7 we mentioned the surprising result that estimates of the stress-corrosion index reported separately by Atkinson [3] and Swanson [32] for Westerly granite and Ralston basalt using samples cut from the same blocks were different in the average value by about 50%.

This striking inconsistency can be explained in light of our results. The length to width ratio of the specimens used by Atkinson was $L/W \sim 2-2.5$, whereas Swanson used longer specimens with $L/W \sim 6$. If we observe Figures 6.7, 6.8, 7.3, and 7.4, we find that for low values of L/W, the inclination of the corrective curve $\psi(a)$ is more important and that the central plateau is not well formed. On the contrary, longer specimens present an extended flat region.

In section § 7.5 we showed that the extent of the underestimation of the

stress-corrosion index produced by Evans' method was tight to the local slope of the corrective function $\psi(a)$. Therefore, it is not surprising that Atkinson obtained lower values than Swanson, although both authors claim to have respected the recommended operational range for crack length. In light of these considerations, the values of n reported by Swanson should be more accurate.

8.3 Perspectives

The examination of many aspects of the experimental procedure and the finite-element study of the strain field in the DT specimen allow us to trust in an experimental configuration, for which the boundary conditions and the internal state of strain are known.

In our project this is only the basic hypothesis to start a new stage of experiments aimed at the reproduction of the earthquake Physics in controlled conditions.

The lava rock specimens will be driven to critical conditions and then will be applied a very low strain rate to simulate the tectonic loading in an active zone surrounding a fault.

A system of several piezoelectric transducers will be connected in different positions on the specimen to monitor the arrival of the acoustic waves emitted by the microfracture events connected to damaging of the specimen and the propagation of a macrocrack in the midplane (fault). The signals will be sampled at a very high rate ($\sim$ 5 MHz) through a powerful digital acquisition system and stored in real time on a hard disk.

The basic methods of seismology will then be used to invert the space and time location of the events, along with their "magnitude". The resulting catalog will be used to perform statistic analysis on the interevent times and on the frequency-magnitude distribution.

The aim of this study is to investigate whether the Gutenberg-Richter scaling low that is observed at crustal scales extends down to the typical scales of a laboratory. This is very important, since it would be the foundation to transfer to the field the understanding of the seismic source that can be achieved in the laboratory.

Appendix A

Corrective Coefficients ψ and ξ

d_n/d	g_w	nl	a / c	4.5cm	6.5cm	8.5cm	10.5cm	12.5cm
1	0	0	0	0.936	0.962	0.966	0.971	1.039
1	0	0	2	0.861	0.950	0.959	0.963	1.038
1	0	0	4	0.774	0.934	0.949	0.956	1.013
2/3	2	0	0	0.944	0.965	0.971	0.987	1.119
2/3	2	0	2	0.938	0.965	0.971	0.987	1.091
2/3	2	0	4	0.925	0.961	0.968	0.981	1.068
2/3	4	0	0	0.968	0.991	0.997	1.021	1.186
2/3	4	0	2	0.962	0.988	0.995	1.015	1.149
2/3	4	0	4	0.948	0.985	0.992	1.010	1.115
1/2	2	0	0	0.964	0.991	0.999	1.048	1.281
1/2	2	0	2	0.961	0.988	1.000	1.040	1.252
1/2	2	0	4	0.952	0.984	0.997	1.034	1.219
1/2	4	0	0	0.977	1.025	1.047	1.118	1.440
1/2	4	0	2	0.973	1.022	1.044	1.111	1.398
1/2	4	0	4	0.964	1.021	1.040	1.099	1.354
1	0	2	0	0.909	0.961	0.965	0.971	1.039
1	0	2	2	-	0.948	0.961	0.963	1.037
1	0	2	4	-	0.931	0.948	0.954	1.012
2/3	2	2	0	0.929	0.966	0.969	0.989	1.120
2/3	2	2	2	0.921	0.964	0.972	0.988	1.093
2/3	2	2	4	0.897	0.961	0.968	0.978	1.067
2/3	4	2	0	0.952	0.989	0.996	1.017	1.186
2/3	4	2	2	0.941	0.987	0.994	1.018	1.149
2/3	4	2	4	0.911	0.981	0.992	1.009	1.115
1/2	2	2	0	0.961	0.990	0.998	1.046	1.282
1/2	2	2	2	0.955	0.987	0.998	1.041	1.253
1/2	2	2	4	0.944	0.985	0.995	1.035	1.220
1/2	4	2	0	0.976	1.026	1.045	1.119	1.438
1/2	4	2	2	0.970	1.021	1.044	1.113	1.400
1/2	4	2	4	0.958	1.018	1.040	1.098	1.347

Table A.1: The corrective factors ψ for specimens of length $L = 17$ cm and width $W = 6$ cm; d is the specimen thickness, d_n the thickness along the groove, g_w the groove width in mm, nl the notch length in cm, $c = \Delta a/d_n$ the inclination of the crack front. Some data is missing because the curved crack front would cross the initial notch. An estmate of their value may be found in Table A.9 (see § 7.3).

d_n/d	g_w	nl	a / c	4.5cm	6.5cm	8.5cm	10.5cm	12.5cm
1	0	0	0	0.892	0.946	0.976	1.038	1.251
1	0	0	2	0.695	0.898	0.932	0.992	1.205
1	0	0	4	0.562	0.859	0.892	0.944	1.113
2/3	2	0	0	0.904	0.958	0.997	1.095	1.430
2/3	2	0	2	0.876	0.938	0.979	1.066	1.361
2/3	2	0	4	0.845	0.917	0.958	1.039	1.297
2/3	4	0	0	0.921	0.975	1.023	1.138	1.529
2/3	4	0	2	0.891	0.954	1.002	1.112	1.457
2/3	4	0	4	0.856	0.931	0.979	1.079	1.384
1/2	2	0	0	0.937	0.999	1.060	1.221	1.721
1/2	2	0	2	0.918	0.984	1.044	1.195	1.646
1/2	2	0	4	0.894	0.969	1.026	1.166	1.586
1/2	4	0	0	0.960	1.037	1.119	1.338	1.987
1/2	4	0	2	0.935	1.020	1.103	1.303	1.902
1/2	4	0	4	0.912	1.004	1.081	1.269	1.804
1	0	2	0	0.835	0.935	0.973	1.038	1.255
1	0	2	2	-	0.899	0.928	0.986	1.201
1	0	2	4	-	0.861	0.885	0.940	1.114
2/3	2	2	0	0.856	0.951	0.995	1.096	1.424
2/3	2	2	2	0.836	0.931	0.975	1.067	1.362
2/3	2	2	4	0.799	0.908	0.953	1.037	1.298
2/3	4	2	0	0.874	0.967	1.019	1.140	1.524
2/3	4	2	2	0.847	0.943	1.000	1.110	1.459
2/3	4	2	4	0.805	0.920	0.977	1.078	1.387
1/2	2	2	0	0.908	0.991	1.061	1.221	1.714
1/2	2	2	2	0.883	0.977	1.045	1.190	1.647
1/2	2	2	4	0.856	0.960	1.027	1.167	1.579
1/2	4	2	0	0.924	1.030	1.120	1.339	1.988
1/2	4	2	2	0.897	1.012	1.100	1.304	1.903
1/2	4	2	4	0.865	0.992	1.083	1.270	1.806

Table A.2: The corrective factors ψ for specimens of length $L = 17$ cm and width $W = 10$ cm.

d_n/d	g_w	nl	a c	5.5cm	8.5cm	12.5cm	16.5cm	20.5cm
1	0	0	0	0.956	0.966	0.965	0.967	1.046
1	0	0	2	0.922	0.960	0.964	0.965	1.040
1	0	0	4	0.892	0.951	0.956	0.956	1.022
2/3	2	0	0	0.960	0.967	0.968	0.974	1.127
2/3	2	0	2	0.960	0.969	0.966	0.975	1.092
2/3	2	0	4	0.953	0.965	0.967	0.970	1.068
2/3	4	0	0	0.984	0.991	0.992	0.992	1.185
2/3	4	0	2	0.983	0.991	0.992	1.000	1.146
2/3	4	0	4	0.977	0.987	0.992	0.993	1.127
1/2	2	0	0	0.983	0.985	0.991	1.001	1.275
1/2	2	0	2	0.982	0.985	0.989	1.003	1.242
1/2	2	0	4	0.976	0.982	0.986	0.999	1.219
1/2	4	0	0	1.018	1.016	1.022	1.048	1.448
1/2	4	0	2	1.014	1.019	1.022	1.044	1.389
1/2	4	0	4	1.009	1.016	1.018	1.038	1.348
1	0	2	0	0.951	0.965	0.965	0.966	1.041
1	0	2	2	-	0.960	0.962	0.960	1.043
1	0	2	4	-	0.946	0.955	0.956	1.020
2/3	2	2	0	0.961	0.967	0.966	0.975	1.128
2/3	2	2	2	0.956	0.968	0.968	0.976	1.093
2/3	2	2	4	0.949	0.967	0.965	0.971	1.069
2/3	4	2	0	0.983	0.991	0.991	1.000	1.187
2/3	4	2	2	0.980	0.990	0.991	0.997	1.148
2/3	4	2	4	0.968	0.987	0.988	0.996	1.121
1/2	2	2	0	0.984	0.990	0.989	1.008	1.276
1/2	2	2	2	0.982	0.986	0.986	1.004	1.242
1/2	2	2	4	0.976	0.983	0.987	0.994	1.220
1/2	4	2	0	1.016	1.023	1.024	1.049	1.439
1/2	4	2	2	1.014	1.016	1.020	1.045	1.390
1/2	4	2	4	1.007	1.014	1.020	1.039	1.349

Table A.3: The corrective factors ψ for specimens of length $L = 25$ cm and width $W = 6$ cm.

d_n/d	g_w	nl	a c	5.5cm	8.5cm	12.5cm	16.5cm	20.5cm
1	0	0	0	0.929	0.962	0.966	0.983	1.251
1	0	0	2	0.841	0.913	0.937	0.946	1.203
1	0	0	4	0.775	0.883	0.898	0.914	1.118
2/3	2	0	0	0.937	0.964	0.972	1.005	1.430
2/3	2	0	2	0.915	0.950	0.958	0.983	1.343
2/3	2	0	4	0.891	0.932	0.939	0.972	1.304
2/3	4	0	0	0.951	0.978	0.982	1.019	1.537
2/3	4	0	2	0.927	0.959	0.966	1.008	1.427
2/3	4	0	4	0.901	0.942	0.953	0.987	1.382
1/2	2	0	0	0.965	0.981	0.987	1.056	1.711
1/2	2	0	2	0.948	0.973	0.985	1.047	1.631
1/2	2	0	4	0.932	0.959	0.970	1.029	1.586
1/2	4	0	0	0.981	1.004	1.014	1.118	1.974
1/2	4	0	2	0.965	0.990	1.002	1.098	1.862
1/2	4	0	4	0.949	0.978	0.987	1.089	1.801
1	0	2	0	0.905	0.959	0.963	0.976	1.254
1	0	2	2	-	0.908	0.936	0.949	1.205
1	0	2	4	-	0.876	0.895	0.917	1.109
2/3	2	2	0	0.922	0.963	0.967	0.995	1.431
2/3	2	2	2	0.901	0.946	0.959	0.984	1.344
2/3	2	2	4	0.872	0.927	0.940	0.973	1.305
2/3	4	2	0	0.932	0.974	0.983	1.020	1.522
2/3	4	2	2	0.911	0.959	0.967	1.010	1.444
2/3	4	2	4	0.881	0.940	0.954	0.989	1.383
1/2	2	2	0	0.950	0.985	0.988	1.056	1.712
1/2	2	2	2	0.930	0.974	0.979	1.047	1.631
1/2	2	2	4	0.912	0.960	0.971	1.029	1.587
1/2	4	2	0	0.967	1.001	1.015	1.118	1.975
1/2	4	2	2	0.947	0.987	1.003	1.099	1.883
1/2	4	2	4	0.927	0.972	0.995	1.078	1.802

Table A.4: The corrective factors ψ for specimens of length $L = 25$ cm and width $W = 10$ cm.

d_n/d	g_w	nl	a / c	$4.5cm$	$6.5cm$	$8.5cm$	$10.5cm$	$12.5cm$
1	0	0	0	1.101	1.057	1.036	1.023	1.018
1	0	0	2	0.892	0.902	0.916	0.925	0.936
1	0	0	4	0.752	0.787	0.827	0.853	0.875
2/3	2	0	0	1.221	1.141	1.100	1.077	1.069
2/3	2	0	2	1.156	1.095	1.065	1.047	1.042
2/3	2	0	4	1.081	1.042	1.024	1.014	1.013
2/3	4	0	0	1.285	1.192	1.145	1.118	1.110
2/3	4	0	2	1.215	1.143	1.107	1.087	1.082
2/3	4	0	4	1.134	1.085	1.062	1.050	1.049
1/2	2	0	0	1.395	1.267	1.198	1.159	1.150
1/2	2	0	2	1.354	1.238	1.175	1.141	1.132
1/2	2	0	4	1.304	1.202	1.148	1.118	1.111
1/2	4	0	0	1.513	1.365	1.282	1.238	1.233
1/2	4	0	2	1.471	1.334	1.258	1.218	1.213
1/2	4	0	4	1.412	1.292	1.226	1.191	1.186
1	0	2	0	1.111	1.063	1.040	1.026	1.021
1	0	2	2	-	0.907	0.920	0.929	0.939
1	0	2	4	-	0.793	0.831	0.856	0.877
2/3	2	2	0	1.224	1.143	1.101	1.077	1.070
2/3	2	2	2	1.159	1.096	1.066	1.048	1.043
2/3	2	2	4	1.086	1.043	1.025	1.015	1.013
2/3	4	2	0	1.290	1.195	1.147	1.119	1.112
2/3	4	2	2	1.221	1.146	1.109	1.088	1.083
2/3	4	2	4	1.142	1.088	1.065	1.052	1.050
1/2	2	2	0	1.397	1.268	1.199	1.160	1.151
1/2	2	2	2	1.356	1.239	1.176	1.141	1.133
1/2	2	2	4	1.306	1.203	1.148	1.118	1.111
1/2	4	2	0	1.516	1.366	1.283	1.239	1.233
1/2	4	2	2	1.474	1.335	1.259	1.219	1.213
1/2	4	2	4	1.416	1.293	1.227	1.191	1.187

Table A.5: The corrective factors ξ for specimens of length $L = 17$ cm and width $W = 6$ cm; d is the specimen thickness, d_n the thickness along the groove, g_w the groove width in mm, nl the notch length in cm, $c = \Delta a/d_n$ the inclination of the crack front. Some data is missing because the curved crack front would cross the initial notch. An estmate of their value may be found in Table A.9 (see § 7.3).

d_n/d	g_w	nl	a / c	$4.5cm$	$6.5cm$	$8.5cm$	$10.5cm$	$12.5cm$
1	0	0	0	1.085	1.037	1.020	1.016	1.034
1	0	0	2	0.764	0.783	0.819	0.850	0.891
1	0	0	4	0.615	0.659	0.719	0.767	0.815
2/3	2	0	0	1.223	1.135	1.098	1.086	1.108
2/3	2	0	2	1.103	1.048	1.029	1.029	1.054
2/3	2	0	4	1.010	0.979	0.975	0.983	1.012
2/3	4	0	0	1.289	1.186	1.142	1.128	1.154
2/3	4	0	2	1.166	1.096	1.071	1.068	1.098
2/3	4	0	4	1.067	1.023	1.013	1.020	1.052
1/2	2	0	0	1.456	1.305	1.235	1.210	1.238
1/2	2	0	2	1.381	1.251	1.192	1.173	1.202
1/2	2	0	4	1.313	1.201	1.153	1.140	1.169
1/2	4	0	0	1.595	1.414	1.330	1.303	1.343
1/2	4	0	2	1.518	1.358	1.285	1.265	1.305
1/2	4	0	4	1.442	1.301	1.240	1.225	1.265
1	0	2	0	1.101	1.042	1.022	1.018	1.035
1	0	2	2	-	0.788	0.822	0.853	0.892
1	0	2	4	-	0.665	0.723	0.769	0.817
2/3	2	2	0	1.232	1.137	1.099	1.087	1.108
2/3	2	2	2	1.113	1.051	1.030	1.029	1.055
2/3	2	2	4	1.021	0.982	0.976	0.983	1.012
2/3	4	2	0	1.301	1.189	1.143	1.129	1.154
2/3	4	2	2	1.178	1.100	1.072	1.069	1.099
2/3	4	2	4	1.082	1.027	1.015	1.021	1.053
1/2	2	2	0	1.461	1.306	1.235	1.210	1.239
1/2	2	2	2	1.387	1.252	1.192	1.174	1.203
1/2	2	2	4	1.320	1.203	1.153	1.140	1.170
1/2	4	2	0	1.602	1.415	1.330	1.303	1.344
1/2	4	2	2	1.526	1.359	1.286	1.265	1.305
1/2	4	2	4	1.451	1.304	1.241	1.226	1.265

Table A.6: The corrective factors ξ for specimens of length $L = 17$ cm and width $W = 10$ cm.

d_n/d	g_w	nl	a / c	$5.5cm$	$8.5cm$	$12.5cm$	$16.5cm$	$20.5cm$
1	0	0	0	1.075	1.036	1.014	1.003	0.998
1	0	0	2	0.894	0.915	0.932	0.940	0.948
1	0	0	4	0.763	0.827	0.871	0.894	0.911
2/3	2	0	0	1.173	1.100	1.057	1.036	1.029
2/3	2	0	2	1.119	1.064	1.033	1.017	1.013
2/3	2	0	4	1.056	1.024	1.005	0.996	0.995
2/3	4	0	0	1.230	1.144	1.094	1.069	1.063
2/3	4	0	2	1.172	1.106	1.069	1.050	1.045
2/3	4	0	4	1.104	1.062	1.039	1.027	1.025
1/2	2	0	0	1.321	1.196	1.123	1.087	1.079
1/2	2	0	2	1.287	1.174	1.108	1.075	1.069
1/2	2	0	4	1.244	1.146	1.089	1.061	1.055
1/2	4	0	0	1.429	1.278	1.189	1.145	1.142
1/2	4	0	2	1.393	1.254	1.173	1.133	1.130
1/2	4	0	4	1.343	1.222	1.151	1.116	1.113
1	0	2	0	1.081	1.040	1.016	1.005	1.000
1	0	2	2	-	0.919	0.934	0.942	0.950
1	0	2	4	-	0.831	0.873	0.896	0.912
2/3	2	2	0	1.175	1.101	1.058	1.036	1.030
2/3	2	2	2	1.121	1.065	1.034	1.018	1.013
2/3	2	2	4	1.059	1.025	1.006	0.997	0.995
2/3	4	2	0	1.233	1.146	1.096	1.070	1.064
2/3	4	2	2	1.175	1.109	1.070	1.051	1.046
2/3	4	2	4	1.108	1.064	1.040	1.028	1.026
1/2	2	2	0	1.322	1.197	1.124	1.087	1.080
1/2	2	2	2	1.288	1.174	1.109	1.075	1.069
1/2	2	2	4	1.245	1.147	1.090	1.061	1.056
1/2	4	2	0	1.431	1.279	1.190	1.146	1.142
1/2	4	2	2	1.395	1.255	1.174	1.134	1.131
1/2	4	2	4	1.345	1.223	1.152	1.117	1.114

Table A.7: The corrective factors ξ for specimens of length $L = 25$ cm and width $W = 6$ cm.

d_n/d	g_w	nl	a c	$5.5cm$	$8.5cm$	$12.5cm$	$16.5cm$	$20.5cm$
1	0	0	0	1.054	1.018	1.002	0.996	1.010
1	0	0	2	0.765	0.815	0.861	0.889	0.922
1	0	0	4	0.626	0.717	0.791	0.835	0.875
2/3	2	0	0	1.168	1.093	1.054	1.036	1.055
2/3	2	0	2	1.067	1.025	1.007	1.000	1.022
2/3	2	0	4	0.987	0.971	0.970	0.972	0.996
2/3	4	0	0	1.225	1.134	1.086	1.065	1.087
2/3	4	0	2	1.120	1.064	1.038	1.028	1.054
2/3	4	0	4	1.036	1.007	0.998	0.998	1.025
1/2	2	0	0	1.362	1.221	1.142	1.107	1.135
1/2	2	0	2	1.300	1.179	1.113	1.085	1.114
1/2	2	0	4	1.242	1.140	1.087	1.065	1.093
1/2	4	0	0	1.479	1.304	1.205	1.165	1.206
1/2	4	0	2	1.414	1.260	1.175	1.142	1.184
1/2	4	0	4	1.350	1.217	1.146	1.119	1.158
1	0	2	0	1.063	1.020	1.004	0.997	1.010
1	0	2	2	-	0.818	0.863	0.890	0.923
1	0	2	4	-	0.722	0.793	0.837	0.876
2/3	2	2	0	1.173	1.094	1.054	1.036	1.055
2/3	2	2	2	1.072	1.026	1.007	1.001	1.022
2/3	2	2	4	0.993	0.972	0.970	0.972	0.996
2/3	4	2	0	1.230	1.136	1.087	1.065	1.088
2/3	4	2	2	1.127	1.066	1.038	1.028	1.054
2/3	4	2	4	1.044	1.009	0.999	0.998	1.026
1/2	2	2	0	1.365	1.221	1.142	1.108	1.135
1/2	2	2	2	1.303	1.179	1.113	1.085	1.114
1/2	2	2	4	1.246	1.141	1.087	1.065	1.093
1/2	4	2	0	1.483	1.304	1.206	1.165	1.206
1/2	4	2	2	1.418	1.261	1.176	1.142	1.184
1/2	4	2	4	1.354	1.218	1.146	1.119	1.158

Table A.8: The corrective factors ξ for specimens of length $L = 25$ cm and width $W = 10$ cm.

L	17cm	17cm	17cm	17cm	25cm	25cm	25cm	25cm
W	6cm	6cm	10cm	10cm	6cm	6cm	10cm	10cm
c	2	4	2	4	2	4	2	4
ξ	0.895	0.756	0.772	0.624	0.896	0.765	0.769	0.631
ψ	0.849	0.756	0.657	0.520	0.920	0.890	0.825	0.755

Table A.9: The corrective coefficients ξ and ψ reported here were estimated to fill the gaps in Tables A.1-A.8.

Bibliography

[1] ASTM E399. Standard Method of Test for Plane Strain Fracture Toughness of Metallic Materials. Annual book of ASTM standards. Designation E399-74. *Am. Soc. Testing Materials*, Philadelphia.

[2] Atkinson B. K., 1979. Technical note. *Int. J. Rock Mech. Min. Sci. & Geomech. Abstr.*, **16**, pp. 49–53.

[3] Atkinson B. K., 1984. Subcritical crack growth in geological materials. *J. Geophys. Res.*, **89**, pp. 4077–4114.

[4] Atkinson B. K., 1987. Fracture mechanics of rock. Academic Press.

[5] Calanchi N., Rossi P. L., Sanmarchi F., Tranne C. A., 1996. Guida escursionistico vulcanologica delle isole Eolie. Centro Studi e Ricerche di Storia e Problemi Eoliani.

[6] Charles R. J., 1958. Static fatigue of glass. *J. Appl. Phys.*, **29**, pp. 1549–1560.

[7] Ciccotti M., Negri N., Sassi L., Gonzato G., and Mulargia F.. Elastic and fracture parameters of Etna, Vulcano and Stromboli lava rocks. *J. Vulc. Geoth. Res.*. Accepted 5 November 1999. In press.

[8] Ciccotti M.. A realistic finite-element model for the Double Torsion loading configuration. Submitted to *J. Am. Ceram. Soc.* in June 1999.

[9] Ciccotti M., Gonzato G., and Mulargia F.. The Double Torsion loading configuration for fracture propagation: an improved methodology for the load relaxation at constant displacement. Submitted to *Int. J. Rock Mech. and Mining Sciences* in December 1999.

[10] Evans A. G., 1972. A method for evaluating the time-dependent failure characteristics of brittle materials—and its applications to polycrystalline alumina. *J. Mater. Sci.*, **7**, pp. 1137–1146.

[11] Evans A. G., Linzer M., Russell L. R., 1974. *Material Science and Engineering*, **15**, pp. 253–409.

[12] Fuller E. R. Jr., 1979. An Evaluation of Double-Torsion Testing—Analysis. In *Fracture Mechanics Applied to Brittle Materials*, ASTM STP 678. *Am. Soc. Testing Materials*, pp. 3–18.

[13] Griffith A. A., 1920. *Phil. Trans. R. Soc. Lond.* **A221**, pp. 163–198.

[14] Irwin G. R., Kies J. A., 1954. Subcritical Crack Growth in Vitreous Carbon at Room Temperature. *Welding Res. Suppl.*, **33**, pp. 193s–198s.

[15] Irwin G. R., 1958. In "Handbuch der Physik. v. VI Elasticity and Plasticity" (ed. Flügge, S.). Springer. Berlin, pp. 551–590.

[16] Jaeger J. C. and Cook N. G. W., 1976. Fundamentals of rock mechanics. 2^{nd} edn., Chapman and Hall, London, p. 585.

[17] Knott J. F., 1973. Fundamentals of Fracture Mechanics. Butterworth, London.

[18] Lawn B. R., 1983. *J. Am. Ceram. Soc.*, **66**, pp. 83–91.

[19] Lawn B. R. and Wilshaw T. R., 1975. Fracture of Brittle Solids. Cambridge University Press. Cambridge, 204 pp.

[20] Liebowitz H., 1968. *FRACTURE An Advanced Treatise VOLUME I Microscopic and Macroscopic Fundamentals*, Academic Press.

[21] Negri N., 1998. *Caratterizzazione dei parametri morfologici, chimici, elastici e di frattura di lave eoliane*, Tesi di Laurea, Università di Bologna.

[22] Ouchterlony F., 1982. *SM Archives* **7**, 131-211. (Also available as Report DS1980:15, SveDeFo, Swedish Detonic Research Foundation, Stockholm, Sweden, 80 pp., 1980.)

[23] Ouchterlony F., 1983. Rock Fracture Mechanics. CISM Courses and Lectures No. 275, (ed: Rossmanith, H. P.), Springer, Vienna, pp. 69–150.

[24] Ouchterlony F., 1986. Evaluation formulas for rock fracture toughness testing with standard core specimens. Presented to SEM Spring Conf., New Orleans, Louisiana, June 9-13.

[25] Pabst R. F., Weick J., 1981. Double torsion measurements with and without a guiding notch. *J. of Materials Science*, **16**, pp. 836–838.

[26] Pletka B. J., Fuller E. R. Jr., and Koepke B. G., 1979. An Evaluation of Double-Torsion Testing—Experimental. In *Fracture Mechanics Applied to Brittle Materials*, ASTM STP 678. *Am. Soc. Testing Materials*, pp. 19–37.

[27] Pollet J. C., Burns S. J., 1979. Crack Velocity Correction Factor for the Crack-Front Shape in Double-Torsion Specimens. *J. Am. Ceram. Soc.*, **62**, pp. 426–427.

[28] Rice J. R., 1978. *J. Mech. Phys. Solids* **26**, pp. 61–78.

[29] Sassi L., 1997. *Vincoli sperimentali di Meccanica delle Fratture sulla determinazione della pericolosità sismica*, Tesi di Laurea, Università di Bologna.

[30] Schmidt R. A. and Lutz T. J., 1979. Fracture mechanics applied to brittle materials. ASTM STP 678, *Am. Soc. Testing Materials*, Philadelphia, pp. 166–182.

[31] Shetty D. K., Virkar A. V., 1978. Determination of the Useful Range of Crack Length in Double Torsion Specimens. *J. Am. Ceram. Soc.*, **61**, pp. 93–94.

[32] Swanson P. L., 1984. Subcritical Crack Growth and Other Time – and Environment – Dependent Behavior in Crustal Rocks. *Journ. Geoph. Res.*, **89**, B6, pp. 4137–4152.

[33] Timoshenko S., Goodier J. N., 1951. Theory of elasticity. McGraw Hill, New York. 2d ed., p. 277.

[34] Trantina G. G., 1977. Stress Analysis of the Double Torsion Specimen. *J. Am. Ceram. Soc.*, **60**, pp. 338–341.

[35] Virkar A. V., Gordon R. S., 1975. Crack Front Profiles in Double-Torsion Specimens. *J. Am. Ceram. Soc.*, **58**, pp. 536–537.

[36] Williams D. P., Evans A. G., 1973. A simple method for studying slow crack growth. *J. Test. Eval.*, **1**, pp. 264–270.